UNIVERSITEIT VAN PRETORIA
UNIVERSITY OF PRETORIA
YUNIBESITHI YA PRETORIA

Surface roughness of InP after N_2^+ bombardment: Ion areic dose dependence

by

Sarah Omer Siddig Osman

Submitted in partial fulfilment of the requirements for the degree

Magister Scientiae

In the faculty of Natural and Agricultural Sciences

University of Pretoria

February 2004

© University of Pretoria

UNIVERSITEIT VAN PRETORIA
UNIVERSITY OF PRETORIA
YUNIBESITHI YA PRETORIA

Surface roughness of InP after N_2^+ bombardment: Ion areic dose dependence

by

Sarah Omer Siddig Osman

Supervisor : J. B. Malherbe

Co-supervisor: N. G. van der Berg

Faculty : Natural and Agricultural Sciences

Department : Physics

Degree : Magister Scientiae

Abstract

Ion beam modification of surfaces has long fascinated the scientific community. It had been observed that bombarding the surfaces with energetic ions usually resulted in the development of topographical features. In the earlier days scientists were interested in studying and understanding this phenomena and how to control it and, in most cases, to reduce this effect. The reason for that is, the increase in the surface roughness leads in the majority of cases to deterioration in the functionality of the thin films contact application and in depth profiling.

InP is a III-V compound semiconductor widely used in optoelectronic and microwave communication systems. These systems require compact components, which can be produced only by micro-fabrication. In micro-fabrication techniques ion bombardment is used for thinning and doping substrates. InP had been of great interest in this field for many reasons. One of them being the dramatic change it exhibits after ion bombardment. It is known that nitrogen implantation induces high resistivity layers on InP with high thermal stability.

InP(100) surfaces were sputtered under ultra high vacuum conditions by N_2^+ at an angle of incidence of 41^o to the sample normal. Energy of 5 keV and areic doses (Φ) of $1X10^{14}$ to $1 X 10^{18}$ N_2^+ /cm^2 were used. InP surface topography development, as a function of N_2^+ areic dose, was investigated using Field Emission Scanning Electron Microscopy (FE-SEM) and Atomic Force Microscopy (AFM).

FE-SEM was used to give a general view of the surfaces. No quantitative work was done on the FE-SEM images. AFM images were quantified in terms of several roughness parameters. Two-dimensional Fourier transforms (FFT) of the AFM images were used to investigate the beginning and the development of the periodicity of the topographical features.

For very low areic doses no change in the surfaces was observed in comparison with recordings for the un-bombarded samples. The starting of cone formation was observed at $\Phi \geq 5 X 10^{15}$ N_2^+ /cm^2. Further increase in the areic dose resulted in the growth in areas and heights of the cones. At an areic dose of $\Phi \geq 5 X 10^{17}$ N_2^+ /cm^2 visible ripples started to appear. These observations were confirmed by the power spectrum (PS) associated with the FFT of the AFM images. The direction of the ripples wave vector was parallel to the surface component of incident ion beam velocity vector in agreement with the Bradley-Harper theory. The wavelength of the surface features was found to depend linearly on the logarithm of the areic dose in the range between $1 X 10^{18}$ N_2^+ /cm$^2 \geq \Phi \geq 5 X 10^{16}$ N_2^+ /cm^2.

A model was proposed for the roughness dependence on the ions areic dose. This model explains the development of the root mean square roughness (R_{rms}) with increasing the areic dose to be a result of two competing processes. The growth of the surface features (cones) is caused by the sputtering effect of the bombarding ions. After a certain areic dose, the erosion of the cones by sputtering would inhibit the growth of cone heights and shapes. The experimental data of the R_{rms} as a function of the areic dose agreed fully with the proposed model.

(524 words)

Acknowledgements

- I would like to thank my supervisor Prof. J. B. Malherbe, without his guidance this work would have not been completed.

- I am very grateful for the cooperation and interest of co-supervisor Dr. N. G. van der Berg for his valuable instructions on the AFM and SEM and image analysis it would have been impossible to proceed with the work without his help.

- I would like to express my gratitude to R. Q. Odendaal for his assistance in samples preparation and sputtering, the work in the AES system and the fruitful discussions.

- I would also like to thank my family for their support.

UNIVERSITEIT VAN PRETORIA
UNIVERSITY OF PRETORIA
YUNIBESITHI YA PRETORIA

Contents

Chapter 6 Discussion

Chapter 7 Conclusion

List of Tables

2.1 *A table showing a summary of surface root mean square roughness (R_{rms}) of InP after O_2^+ bombardment as a function of the angle of incidence first, and then as a function of the incident ion energy ... ...

List of Figures

Chapter 1

An Overview: Nanotechnology, InP, Topography Investigation Techniques

1.1 Introduction

Information technology (IT) is more than a trillion dollar industry and semiconductor technology is at the centre of its development. IT uses semiconductors for a variety of applications including digital, radio frequency (RF), analog and opto-electronic applications. These applications include, for example, optical data transfer, telecommunications, sensors and displays.

In the field of IT the role of semiconductors is becoming particularly important in micro (small scale) technology and microelectronics. As a result, the semiconductor industry is shifting towards nano-chips with less than 0.1-micron features. Consequently, research in this field is in turn shifting from micro to nano scales. Understanding semiconductor physics and the control of materials properties is becoming crucial for improvement of the technology on which our modern life is becoming increasingly built. In development of the nano scale devices, it was found that changes in the properties of the materials occurred. Nano-scale devices attained increased functionality, became easier to integrate and the total cost was lowered.

This new field of nano-fabrication of components necessitates new methods of cleaning and doping. One of the most successful methods is doping by ion implantation. This method is mostly employed in the development of devices that use III-V compound semiconductors.

One of the disadvantages of doping material with ion implantation is the development of surface topographical features that causes deterioration of the quality of the devices. It was observed that these features start to grow under specific conditions and develop into regular features to form nano dots and nano wires (ripple-like structures). This has resulted in a new field of semiconductor nano fabrication.
In some practical applications, a need for surfaces with high roughness values may arise, for example, in catalysis application (the larger the surface area the more efficient the catalysis).

Generally speaking, the study of solid surfaces requires using surface sensitive techniques such as SIMS, XPS and AES combined with inert gas ion sputtering. The quality and accuracy of the results of these techniques can be expressed in term of the so-called depth resolution. It has been observed that the quality of the depth resolution deteriorates with increasing surface roughness. Attempting to increase depth profile resolution was the reason for investigating the mechanisms of surface roughening.

Most of the reported results of the bombardment-induced topography dealt with inert gas ion bombardment. The morphology of surfaces bombarded with energetic ions has long fascinated the experimental community. Recently, and with the development of high-resolution observation techniques such as atomic force and scanning tunneling microscopies, this problem is getting more attention and it is intensively being studied.

1.2 InP (Indium Phosphate) an Extreme Example

In this study InP substrates were used for two reasons, firstly, because of the dramatic change in topography after ion bombardment at room temperature, secondly, because of the importance of the InP as a material in devices.
For example, InP is used in solar cell fabrication, where the near optimum spectral response of InP, plus its superior resistance to radiation damage, combines to make it the best available choice. In addition, it is used for power generation in space vehicles, in microwave applications as a transistor or as a Gunn effect oscillator and in integrated optics. In other applications, it is used for its opto-electronic properties. Another of its important functions is in the InP transferred electron devices.

Why Nitrogen?

The importance of III-V nitrides for semiconductor devices and their application in the blue and ultraviolet wavelength [Str 92] was one of the key reasons for their recent scientific interest. InN in particular, with a direct band gap of 1.9 eV, has a potential use in low cost, highly efficient optoelectroinc devices such as solar cells and semiconductor lasers [San 03]. Nitrogen implantation into materials has many technological applications. Nitrogen has been used to create high resistivity layers in InP by ion implantation. Using this technique on semi-insulating InP, it is possible to create a semiconductor-on-insulator structure to be used as a substrate for further device fabrication [Xio 89]. Nitrogen implantation-induced high resistivity layers has better thermal stability.

The experimental investigation can be classified into two main groups. First, early investigations [Bar 73], [Vas 75] and a number of recent studies [Kar 91], [Kar 95], [Mac 92] and [Cha 94] have found sputter eroded surfaces develop a ripple morphology which has a characteristic wavelength in the order of few micrometers. However, a number of research groups have found no evidence of ripples, but observed the development of apparently rough surfaces that were characterized using scaling theories [Mak 02].

One of the most important parameters in bombardment-induced topography is the ions areic dose as it controls the number of particles bombarding the surface, thus the energy deposited on the surface of the sample.

1.3 The Techniques Used in this Study

Traditionally, the Scanning Electron Microscopy (SEM) had been the favourite technique to investigate topography of substrates and to a lesser extent, the Transmission Electron Microscopy (TEM). After the invention of the Scanning Probe Microscopy (SPM) in the 1980's, it became the most appropriate technique to investigate the surface morphology with a very high (nanometre scale) resolution and obtaining quantitative information such as the roughness of the surfaces, dimensions of sputter craters, etc.

In this study Field Emission Scanning Electron Microscopy (FE-SEM) is used to investigate the substrates and to give an idea of the overall surface. Atomic Force Microscopy (AFM) is used to investigate the surface and to quantitatively

characterize the surfaces under different sputtering conditions. Interpretations from both techniques are presented here.

1.4 Aim of the Study

This study is aimed at exploring the effect of nitrogen ion bombardment on the topography of the compound semiconductor InP. The dependence of surface topography (roughness and the development of periodic structures) on areic dose will be investigated, and a comparison of the two techniques used will also be made.

References: Chapter 1

[Bar 73] D.J. Barber, F.C. Frank, M. Moss, J.W. Steeds and I.S. Tsong, *J. Mater. Sci.* 8 (1973) 1030.

[Cha 94] E. Chason, T. M. Mayer, B. K. Kellerman, D. T. McIlroy and A. J. Howard, *Phys. Rev. Lett.* 72 (1994) 3040.

[Kar 91] A. Karen, K. Okuno, F. Soeda and A. Ishitani, *J. Vac. Sci. Technol.* A 9 (1991) 2247.

[Kar 95] A. Karen, Y. Nakagawa, M. Hatada, K. Okuno, F. Soeda and A. Ishitani, *Surf. Interface Anal.* 23 (1995) 506.

[Mac 92] S. W. MacLaren, J. E. Baker, N. L. Finnegan and C. M. Loxton, *J. Vac. Sci. Technol.* A 10 (3) (1992) 468.

[Mak 02] M. A. Makeev, R. Cuerno and A.- L. Barabasi, *Nucl. Instrum. Meth. Phys. Res.* B 197 (2002) 185.

[San 03] K. Santhakumar, R. Kesavamoorthy, K. G. M. Nair, P. Jayavel, D. Kanjilal, V. Sankara Sastry and V. Ravichandran, *Nucl. Instrum. Meth. Phys. Res.* B 212 (2003) 521.

[Str 92] S. Strite and H. Morkoc, *J. Vac. Sci. Technol.* B 10 (1992) 1237.

[Vas 75] F. Vasiliu, I.A. Teodorescu and F. Glodeanu, *J. Mater. Sci.* 10 (1975) 399.

[Xio 89] F. Xiong, T. A. Tombrello, T. R. Chen, H. Wang, Y. H. Zhuang and Y. Yariv, *Nucl. Instrum. Meth. Phys. Res.* B 39 (1989) 487.

Chapter 2

Sputtering by Particle Bombardment

2.1 Introduction to Sputtering

Sputtering of solids is the emission of surface atoms upon impact of energetic particles or ion radiation [Hof 76]. Sputtering has also been defined as the erosion on the surface of a solid as a consequence of energetic particle bombardment that is observable in the limit of small particle current and areic doses [Sig 81]. Sputtering presents several variants known as chemical, collisional, thermal, electronic, and exfoliational sputtering [Kel 84].

If a beam of energetic ions impinges on a solid, several processes involving the ions happen in the area of interaction;
-A fraction of the incident ions will be back scattered from the surface layer.
- Another fraction is slowed down in the solid and may be trapped or may diffuse to the surface or into the bulk.
- If the energy of the incident ions is high enough and the substrate is a thin film, some of the incident ions will be transmitted.
- Electron, photons, ions may be emitted and atoms from the solid may be released at the surface i.e. sputtered [Beh 83].

The erosion due to sputtering is quantified by the sputter yield (Y), which is defined as the mean number of atoms removed from the surface of the target per unit incident particle [Beh 83].

Y = the number of emitted (sputtered) atoms/ the number of incident ions

The sputter yield depends on the structure, composition of the target material, the parameters of the incident ion beam and the experimental geometry [Fel 86].

If an incident ion with sufficient energy collides with an atom of the solid, it can create a primary knock-on atom. For a collision cascade, started by this primary knock-on atom several regimes must be considered;

The single knock-on regime

The single knock-on regime applies to low ion energy bombardment (close to the threshold ~ 8.2 ev for P in InP), where mostly only small energies are transferred to the target atom. In this regime only few collisions can occur, and the primary knock-on atoms contribute significantly to the sputtering.

The linear cascade regime

For bombardment with ions of medium to high atomic numbers in the keV energy region large collision cascades can develop. When a cascade intersects with the surface, sputtering of the target atoms can occur. In this regime, moving target atoms collides only with target atoms at rest.

The spike regime

In this regime many of the binary collisions between target atoms happen when both are moving. The cascade leading to the sputtering in this case is very dense. A major part of the atoms within the cascade volume are released from their lattice sites and set in motion.

In crystalline materials the probability of collisions of the incoming ions to create a knock-on atom as well as the development of collision cascades are, in addition, influenced by the crystal structure due to channelling, blocking or shadowing and focusing effects [Beh 83].

Multi-component solids often show preferential sputtering behaviour. In other words, the partial sputtering yields of the different species are not proportional to their atomic concentration on the surface. Two processes contribute to preferential sputtering. The first is that in the collision cascades the energy is not equally distributed among different mass atoms in the solid. The other is the different binding energies of different atoms at the surface.

The situation is even more complicated when bombarding with chemically reactive ions [Rot 84]. A compound layer may build up with different surface binding energy thus, different sputter yield than the original surface. The atomic processes leading to chemical sputtering consist of several steps such as implantation of reactive ions, compound formation and compound desorption. When bombarding the samples with reactive gas, for example O_2^+ bombardment of SiC, some volatile compounds (CO_2) might form which will be released from the surface. When bombarding non-metals with energetic ions the energy transferred to electronic excitation and ionization may also contribute to sputtering [Beh 83].

The main aspects of ion beam modification of surfaces are structural, topographical, electronic and compositional. This study is concerned mainly with topographical changes. In structural changes, the crystalline phase is amorphized or an amorphous material is re-crystallized. It was observed that ion bombardment causes either amorphization or crystallization of the target, if the dose is high enough [Nag 70]. These structural changes increase with increasing ion mass and areic dose. The removal of atoms from the surface by sputtering does not occur uniformly over the bombarded area. Furthermore, the implanted ions can modify the surface structure. Thus during ion bombardment surface topography develops, which is mostly different from that of the original one. Cones, needle- like structures, grooves, ridges and pyramids and/or blistering, exfoliation and spongy surfaces may develop [Kel 84]. Electronic changes include the consequence of chemical changes due to the composition of the incident beam, carrier injection due to energy deposition, chemical changes due to recoil implantation and chemical changes due to preferential sputtering [Kel 84]. By compositional changes we mean the formation of a surface layer with a different composition than the original surface as a result of ion implantation.

2.2 Bombardment induced topography development: Experimental results

In this section the different experimental results reported for InP and some other III-V semiconductors are presented. The effect of sputtering parameters on the bombardment-induced surface modification is generally reviewed.

2.2.1 Radiation induced topography; InP and other III-V compound semiconductors

The features that develop on InP surfaces bombarded with energetic noble gas ions have long fascinated scientists. From early investigations [Wil 73] done by scanning electron microscopy until the present a number of excellent quantitative measurements of images have been achieved from techniques like atomic force microscopy (AFM) and scanning tunnelling microscopy [San 03a], [San 03b]. The reasons for this scientific curiosity is the dramatic changes that InP develops after ion bombardment at room temperature and the role that InP plays in the semiconductor industry for its near optimum opto-electronic properties (see Chapter 1).

Most of the experimental studies agreed that at the early stages of ion bombardment at room temperature the bombarded surface consist of cones or cone-like features. With increasing the areic dose, the cones develop into needle-like structures and in some case into ripples.

The cones can be divided into two groups [Mal 94a]. The first group appears on as-received from factory InP wafers at a dose of approximately 5×10^{15} ions/cm^2 as small protuberances (~ 10nm) and grow to heights of ~ 10-100 nm with increasing the areic doses. Linders *et. al.* [Lin 86] using O_2^+ and Ar^+ stated that in low energy regime ($E \leq 10$keV) the morphology has only a small dependence on the bombarding ion energy. For Ar^+ bombardment when the angle of incidence was kept fixed at 40^o, slight dependence was observed at 0.5 - 5keV energy ranges. In the same study it was observed that sputtering at lower energies (0.5 - 1 keV) results in increasing the surface roughness in comparison with higher energies [Mal 94b]. Another study [Dem 96a] showed that the roughness behaviour depends on the ion species and for each ion species there is a critical energy for which the surface roughness (R_{rms}) attains a maximum value. At a constant ion energy and areic dose the density and size of these cones depends on the angle of incidence [Hou 85] [Mal 94b], [Dem 96b], [Wad 84].

The second group of cones initially looks like the first group but later develops into spiky or whisker- like features [Gri 89]. It had been shown that this group originates from seeding (re-deposition) from the sample holder impurities [Wad 84], [Mal 94b].

For oblique incidence angles periodic height modulations (ripples) was reported on irradiated surfaces, but some research groups observed only changes in the surface

roughness with no periodicity (see tables 2.1 & 2.2 for InP and table 2.3 for other compound semiconductors). The orientation of the ripples depends on the angle of incidence of the impinging ions (2.2.2.1). Ripples formation is material specific, however, it has been reported for insulators (diamond [Dat 01]), Semiconductors (Si [Car 96], GaAs [Ste 88], InP [Dem 95]) and metals (Ag [Rus 99]).

Recent studies [Kro 03a], [Kro 03b] investigated the InSb (100) surface bombarded with 4 keV Ar^+. They looked at topography evolution from the stage of small dots to the construction of nanowires incorporated to a flat amorphous surface. The nanowires were parallel to the projection of ion beam with diameters of few tens of nanometres.

No ripples were observed after oxygen bombardment of InP to areic dose of 3 $x10^{17}$ ions/ cm^2 [Pan 98].

Table 2.1: *A table showing a summary of surface root mean square roughness (R_{rms}) of InP after O_2^+ bombardment as a function of the angle of incidence first, and then as a function of the incident ion energy.*

Material	Ion type	Angle of incidence (deg)	Ion energy (keV)	R_{rms} (μm)	Ref.
InP	O_2^+	0	6	20	[Pan 98]
InP	O_2^+	15	6	25	[Pan 98]
InP	O_2^+	30	6	28	[Pan 98]
InP	O_2^+	47	6	30	[Pan 98]
InP	O_2^+	60	6	26	[Pan 98]
InP	O_2^+	75	6	18	[Pan 98]
InP	O_2^+	45	2	17	[Pan 98]
InP	O_2^+	45	4	22	[Pan 98]
InP	O_2^+	45	6	30	[Pan 98]
InP	O_2^+	45	10	28	[Pan 98]

2.2.1.1 InP topography dependence on ion areic dose

Most of the experimental studies of cones and ripples growth addresses the dependence on incidence angle, ion energy, areic dose rate and sample temperature. Studies of the areic dose dependence are rare and contradictory [Erl 99], [Vaj 96], [Liu 01], and [Dem 95]. Most of the reported results on InP bombardment induced topography were for noble gas ion bombardment. Very few experimental studies dealt with reactive ions [Dun 84], [San 03a], [San 03b], [Pan 98].

In table 2.2 some of the experimental results are shown for the development of ion bombarded InP surfaces' topographical features as a function or areic dose.

Table 2.2: *A summary of experimental results of the root mean square roughness R_{rms} (μm) and the ripple's wavelength λ (nm) of Ar^+ bombarded InP (100) as a function of areic dose (ions/cm²).*

Material	Ion type	Angle of incidence (deg)	Ion energy (keV)	Areic dose (ions/cm²)	R_{rms} (μm)	λ (nm)	Ref.
InP(100)	Ar^+	41	0.5	$1x10^{15}$	0.55	-	[Dem 95]
InP(100)	Ar^+	41	0.5	$5x10^{15}$	0.90	-	[Dem 95]
InP(100)	Ar^+	41	0.5	$1x10^{16}$	4	9.3	[Dem 95]
InP(100)	Ar^+	41	0.5	$5x10^{16}$	6.9	12.5	[Dem 95]
InP(100)	Ar^+	41	0.5	$1x10^{17}$	8.6	16	[Dem 95]
InP(100)	Ar^+	41	0.5	$5x10^{17}$	10.5	-	[Dem 95]
InP(100)	Ar^+	41	0.5	$1x10^{18}$	10.5	25	[Dem 95]
InP(100)	Ar^+	71	5	$1x10^{15}$	0.4	-	[Dem 95]
InP(100)	Ar^+	71	5	$5x10^{15}$	1.6	-	[Dem 95]
InP(100)	Ar^+	71	5	$1x10^{16}$	3.1	-	[Dem 95]
InP(100)	Ar^+	71	5	$5x10^{16}$	4.5	-	[Dem 95]
InP(100)	Ar^+	71	5	$1x10^{17}$	4.2	-	[Dem 95]
InP(100)	Ar^+	71	5	$5x10^{17}$	-	-	[Dem 95]
InP(100)	Ar^+	71	5	$5x10^{17}$	-	-	[Dem 95]
InP(100)	Ar^+	71	5	$1x10^{18}$	7	-	[Dem 95]

2.2.1.2 The composition of nitrogen bombardment induced structures on InP surfaces

A number of experimental studies were done to investigate the effect of nitrogen bombardment on InP surfaces. This scientific interest is due to the importance of III-V nitrides $(InP)_xN_y$ for semiconductor devices applications [Str 92].

In a study done by Ren *et. al* [Ren 94], it was reported that N^+ bombarded n- type InP produced indium rich surfaces containing polycrystalline InN.

A study investigating the surface composition and the chemical state of N_2^+ bombarded InP (100) at room temperature using XPS showed that a thin InN layer was formed [Pan 96]. In the same study it was shown that the nitridation degree is energy and angle of incidence dependent. In the range 2-10 keV of ion energy it was found the nitridation degree depends mainly on the angle of incidence.

Recently Santhakumar *et. al.* [San 03a], [San 03b], used ion beam implantation to synthesize InN at high temperature. A 50 keV N^+ beam was used to bombard InP(100) at 400^oC for areic doses 1×10^{14}-1×10^{17} N^+/cm^2. The induced surface structures were investigated using grazing incidence X-ray diffraction (GIXRD) and Raman spectroscopy. For low areic doses the surface consisted of metal enriched InP. By increasing the implantation dose, complete nitridation took place as a result of the disappearance of the metallic indium and the formation of hexagonal phase InN [San 03b].

2.2.2 Ripple formation on semiconductor surfaces

The ripple morphology on ion-bombarded metal and semiconductor surfaces was discovered in the 1970's as was discussed in [Car 83]. Early studies were only concerned about reducing the bombardment induced topographical features, because of the role it plays in the deterioration of depth resolution in surface analytical techniques and implanted thin films quality. Recently, the development of the nanotechnology industry increased the interest for finding new and practical ways of manufacturing nano-dots and nano-wires. It was found that ion induced processes also lead to segregation and self-organization of the surfaces, which sometimes develop into periodic structures [Kro 03b]. The characteristic dimensions of these structures are in the order of nanometres. It is of current interest to understand those

processes and study their dependence on the different sputtering macroscopic parameters in order to tune the final surface morphology.

2.2.2.1 Angle of incidence dependence

A large number of research groups have investigated the effect of the ion incidence angle on ripples. These results indicate that ripples only appear for a limited range of incidence angles depending on the material and the ions involved. The angles reported to produce ripples typically vary between 30^o-60^o [Mak 02]. Below a critical angle θ_c the ripples were found to be perpendicular to the ion beam projection to the surface, while for angles above θ_c it is parallel to the ion beam projection. These results are in agreement with the predictions of Bradley and Harper [Bra 88] and recent Monte Carlo simulation by Koponen [Kop 97a], [Kop 97b].

A study done on InP (100) bombarding it with 0.5 keV Ar^+ and 0.5 and 5 KeV Kr^+ and a fixed areic dose showed that there is a correlation between the dependency of roughness and sputter rate on the angle of ion incidence [Dem 96b]. In the same study it was reported that at 41^o to the sample normal maximum roughness was obtained for the different ion species and ion energies used.

2.2.2.2 Temperature dependence

It was found that the ripples wavelength is strongly influenced by the temperature of the substrate, as was reported by MacLaren *et. al* [Mac 92] from a series of experiments on InP and GaAs bombarded with O_2^+ and Cs^+. In the same study it was observed that at high temperatures the ripple wavelength depends exponentially on the substrate temperature (in agreement with the Bradley Harper theory), while at low temperatures the wavelength was constant.

For crystalline (Si) bombarded with 10-40 keV Xe^+ ions at 45^o Carter *et. al.* [Car 96] reported formation of ripples of 0.4 μm wavelength. Changing the surface temperature from 100-300^{o}K did not affect the ripple wavelength or orientation. The author concluded that the smoothing mechanisms are not of thermal origin.

2.2.2.3 Areic dose rate and areic dose dependence

The effect of ion areic dose (ions/cm^2) on surface dynamics was studied by Chason *et. al.* [Cha 94], [May 94]. Using 1keV Xe^+ to bombard SiO_2 substrates at 55^o with an

ion areic dose rate of 10^{13} ions/cm^2.s and an areic dose up to 1×10^{15} ions/cm^2. Their results showed that the interface roughness, which is proportional to the ripple amplitude, increased linearly with the areic dose.

A similar experiment was done on Ge (100) using 0.3 and 0.5 keV Xe^+ ions and areic dose 6×10^{16} ions/cm^2 and areic dose rate up to 1.9 x10^{13} ions/cm^2 s at T= 350^o C [Cha 96]. Results indicate that the roughness increases as the square of the areic dose rate. The effect of areic dose on the topography of InP was discussed in detail in 2.2.1.1.

2.2.2.4 Ion energy dependence

A number of experimental studies agreed that the ripple wavelength depends linearly on the ion energy [Kar 91], [Kar 95], [Vaj 96], [Dem 96a]. See table 2.3 for more information about the materials used and the sputtering parameters. Carter *et. el.* stated that the ripple wavelength is relatively insensitive to primary ion energy [Car 96].

In a study on InP(100) surfaces, bombarded by Ne^+, Ar^+ and Kr^+ it was reported that for every ion species there is a critical energy for which the surface roughness attains a maximum value [Dem 96a].

2.2.2.5 Ion mass dependence

Bombarding InP with 0.5 keV and 5keV, of He^+, Ne^+, Ar^+, Kr^+ and Xe^+ ions at an angle of incidence of 41^o with a fixed areic dose of 2×10^{17} ions/cm^2, it was found that increasing ion mass results in a pronounced change in the sputter induced topography [Vij 98]. The heights of the sputter cones increased with increasing ion mass up to argon, and then decreased. The cone density increased with increasing ion mass. Using high ion masses, ripples tend to develop as a result of merging cones (Kr^+ onwards).

2.2.2.6 Ripple amplitude and wavelength

Bombardment time evolution of ripple amplitudes is an important factor in studying ripple formation. Experimental results showed that the ripple amplitude at short time scales increases exponentially, but after a short time saturation was observed [Cha 01].

A large number of studies were done to investigate the effect of varying different sputtering parameters on the ripple wavelength. Table 2.3 summarizes some of the experimental results for some non-metallic substrates.

Table 2.3: *A summary of the ripple characteristics reported in some experiments*

Material	Ion type	Angle of incidence (deg)	Ion energy (keV)	Ripple wavelength (μm)	Ref.
GaAs (100)	O_2^+	39	8	0.2	[Ste 88]
GaAs (100)	O_2^+	42	5.5	0.1	[Ste 88]
GaAs (100)	O_2^+	37	10.5	0.23	[Kar 91]
GaAs (100)	O_2^+	42	5.5	0.13	[Kare 95]
GaAs (100)	O_2^+	39	8.0	0.21	[Kar 95]
GaAs (100)	O_2^+	37	10.5	0.27	[Kar 95]
GaAs (100)	O_2^+	57	13	0.33	[Kar 95]
GaAs	O_2^+	40	3.0	0.075	[Cir 91]
GaAs	O_2^+	40	7.0	0.130	[Cir 91]
Ge(001)	Xe^+	55	1	0.2	[Cha 94]
Si(001)	O_2^+	41	6	0.4	[Ste 88]
Si(001)	O_2^+	42	5.5	0.5	[Ste 88]
Si(100)	O_2^+	39	8	0.5	[Ste 88]
Si(100)	O_2^+	40	3	0.198	[Vaj 96]
Si(100)	O_2^+	40	5	0.302	[Vaj 96]
Si(100)	O_2^+	40	9	0.408	[Vaj 96]
Si(100)	Ar^+	67.5	0.75	0.57	[Erl 99]
Si	Xe^+	45	40	0.4	[Car 96]
Si	O_2^+	37	12.5	0.35	[Els 93]
SiO_2	Ar^+	45	0.5-2	0.2-0.55	[Umb 99]
SiO_2	Xe^+	55	1	0.03	[May 94]

In table 2.3 the ripple wave vector is parallel to the ion beam direction. For reported results on the InP see table 2.2.

References: Chapter 2

[Beh 83] R. Behrisch , in *Sputtering by Particle Bombardment II,* R. Behrisch(Ed.), Springer- Verlag, Berlin (1983) Chapter 1.

[Bra 88] R. M. Bradley and J. M. E. Harper, *J. Vac. Sci. Technol.* A 6 (1988) 2390.

[Car 96] G. Carter and V. Vishnyakov, *Phys. Rev.* B 54 (1996) 17647.

[Cha 94] E. Chason, T. M. Mayer, B. M. Kellerman, D. T. McIlroy and A. J. Howard, *Phys. Rev. Lett.* 72 (1994) 3040.

[Cha 96] E. Chason, T. M. Mayer and B. M. Kellerman, *Mat. Res. Soc. Symp. Proc.* 396 (1996) 143.

[Cha 01] E. Chason, J. Erlebacher, M. Aziz, J. A. Floro and M. Sinclair, *Nucl. Instr. Meth. Phys. Res.* B 178 (2001) 55.

[Cir 91] E. H. Cirlin, J. J. Vajo, R. E. Doty and T. C. Hasenberg, *J. Vac. Sci. Technol.* A 9 (1991) 1395.

[Dat 01] A. Datta and Y-R. Wu and Y. L. Wang, *Phys. Rev.* B 63 (2001) 125407.

[Dem 95] C. M. Demanet, J. B. Malherbe, N. G. van der Berg and K. Vijaya Sankar, *Surf. Interface Anal.* 23 (1995) 433.

[Dem 96a] C. M. Demanet, K. Vijaya Sankar, J. B. Malherbe, N. G. van der Berg and R. Q. Odendaal, *Surf. Interface. Anal.* 24 (1996) 497.

[Dem 96b] C. M. Demanet, K. Vijaya Sankar and J. B. Malherbe, *Surf. Interface Anal.* 24 (1996) 503.

[Dun 84] S. Duncan, R. Smith, D. E. Sykes and J. M. Walls, *Vacuum* 34 (1984) 145.

[Els 93] K. Elst, W. Vandervorst, J. Alay, J. Snauwaert and L. Hallemans, *J. Vac. Sci. Technol.* B 11 (1993) 1968.

[Erl 99] J. Erlebacher, M. J. Aziz, E. Chason, M. B. Sinclair and J. A. Floro, *Phys. Rev. Lett.* 82 (1999) 2330.

[Fel 86] L. G. Feldman and J. W. Mayer, in *Fundamentals of Surface and Thin Film Analysis*, Elsevier, New York (1986) Chapter 4.

[Gri 89] W. H. Gries, *Surf. Interface Anal.* 14 (1989) 611.

[Hof 86] W. O. Hofer, in *Erosion and Growth of Solids Stimulated by Atoms and Ion Beams*, G. Kiriakidis (Ed.), G. Carter and J. L. Whitton (1986) Chapter 1.

[Hou 85] X. -Y. Hou, M.– R. Yu and X. Wang, *Chin. Phys. Lett.* 2 (1985) 31.

[Kar 91]A. Karen, K. Okuno, F. Soeda and A. Ishitani, *J. Vac. Sci. Technol.* A 9 (1991) 2247.

[Kar 95] A. Karen, Y. Nakagawa, M. Hatada, K. Okuno, F. Soeda and A. Ishitani, *Surf. Interface Anal.* 23 (1995) 506.

[Kel 84] R. Kelly, in *Ion Bombardment Modification of Surfaces*, O. Auciello and R. Kelly(Ed.), Elsevier, Netherlands (1984) Chapter 2.

[Kop 97a] I. Koponen, M. Hautala, and O.- P. Sievanen, *Phys. Rev. Lett.* 78 (1997) 2612.

[Kop 97b] I. Koponen, M. Hautala, and O.- P. Sievanen, *Nucl. Instrum. Meth. Phys. Res.* B 129 (1997) 349.

[Kro 03a] F. Krok, J. Kolodziej, B. Such, P. Piatkowski and M. Szymonski, *Appl. Surf. Sci.* 210 (2003) 112.

[Kro 03b] F. Krok, J. J. Kolodziej, B. Such, P. Piatkowski and M. Szymonski, *Nucl. Instrum. Meth. Phys. Res.* B , 212 (2003) 264.

[Lin 86] J. Linders, H. Niedrig, T.Sebald and M. Sternberg, *Nucl. Instrum. Meth. Phys. Res.* B 13 (1986) 374.

[Liu 01] Z. X. Liu and P. F. A. Alkemade, *Appl. Phys. Lett.* 79 (2001) 4334.

[Mac 92] S. W. MacLaren, J. E. Baker, N. L. Finnegan and C. M. Loxton, *J. Vac. Sci. Technol.* A 10 (1992) 468.

[Mak 02] M. A. Makeev, R. Cuerno and A.- L. Barabasi, *Nucl. Instrum. Meth. Phys. Res.* B 197 (2002) 185.

[Mal 94a] J. B. Malherbe, *CRC Crit. Rev. Solid State Mater. Sci.* 19 (1994) 129.

[Mal 94b] J. B. Malherbe and N. G. van der Berg, *Surf. Interface Anal.* 22 (1994) 538.

[May 94] T. M. Mayer, E. Chason and A. J. Howard, *J. Appl. Phys.* 76 (1994) 1633.

[Nag 70] H. M. Naguib and R. Kelly, *J. Nucl. Mater.* 35 (1970) 293.

[Pan 96] J. S. Pan, A. T. S. Wee, C. H. A. Huan, H. S. Tan and K. L. Tan, *J. Phys. D: Appl. Phys.* 29 (1996) 2997.

[Pan 98] J. S. Pan, S. T. Tay, C. H. A. Huan and A. T. S. Wee, *Surf. Interface Anal.* 26 (1998) 930.

[Ren 94] F. Ren, S. J. Pearton, J. R. Lothian, S. N. G. Chu, W. K. Chu, R. G. Wilson, C. R. Abernathy and S. S. Pei, *Appl. Phys. Lett.* 65 (1994) 2165.

[Rot 83] J. Roth, in *Sputtering by Particle Bombardment II,* Ed. by R. Behrisch(Ed.), Springer- Verlag, Belin (1983) Chapter 3.

[Rus 99] S. Rusponi, G. Costantini, F. Bautier de Mongeot, C. Boragno and U. Valbusa, *Appl. Phys. Lett.* 75 (1999) 3318.

[San 03a] K. Santhakumar, P. Jayavel, G. L. N. Reddy, V. S. Sastry, K. G. M. Nair and V. Ravichandran, *Nucl. Instrum. Meth. Phys. Res.* B 212 (2003) 197.

[San 03b] K. Santhakumar, R. Kesavamoorthy, K. G. M. Nair, P. Jayavel, D. Kanjilal, V. Sankara Sastry and V. Ravichandran, *Nucl. Instrum. Meth. Phys. Res.* B 212 (2003) 521.

[Sig 81] P. Sigmund, in *Sputtering By Particle Bombardment I*, R. Behrisch (Ed.), Spinger-Verlag, New York (1981) Chapter 2.

[Ste 88] F. A. Stevie, P. M. Kahora, D. S. Simons and P. Chi, *J. Vac. Sci. Technol.* A 6 (1988) 76.

[Str 92] S. Strite and H. Morkoc, *J. Vac. Sci. Technol.* B 10 (1992) 1237.

[Umb 99] C. C. Umbach, R. L. Headrick, B. H. Cooper, J. M. Balkely and E. Chason, *Bull. Am. Phys. Soc.* 44 (1) (1999) 706.

[Vaj 96] J. J. Vajo, R. E. Doty and E. H. Cirlin, *J. Vac. Sci. Technol.* A 14 (1996) 2709.

[Vij 98] K. Vijaya Sankar, in PhD thesis, University of Transkei (1998).

[Wad 84] O. Wada, *J. Phys.* D 17 (1984) 2429.

Chapter 3

THEORETICAL APPROACH TO NANOMETER- SIZED STRUCTURES INDUCED BY ION SPUTTERING

3.1 Introduction

During ion bombardment of semiconductor surfaces, the interaction between the impinging ion and the target atom can induce different effects to the target material, which can be group into three categories: -

- Surface compositional changes.
- Crystal defects, which can lead to electrical, optical, and mechanical changes.
- Topographical changes.

In the 1960s more attention had been given to the first two phenomena and researchers tend to ignore the topographical changes. That was mainly due to lack of applications and the very large variety and random structure that surfaces develop after ion bombardment. The main and most important reason was the lack of quantitative and predictive models [Mal 02].

3.2 Theoretical approaches

The theories and models that explain the bombardment-induced topography can be divided into three main groups [Mal 94b]: -

3.2.1 Sputter erosion theories (sputter yield based models)

(a) Impurity seeding model

This model is a classical explanation of cone formation showing that metal seeded surfaces induce surface morphology after ion bombardment. Two mechanisms are proposed to take place. The first is that impurities having lower sputter yields than its surroundings act as a starting point for cone formation due to faster erosion of its surroundings (see figure 3.1). The surfaces develop into conical protrusions as a result of the variation of sputter yield with the angle of incidence. The main characteristics of these seeded cones are the circular cross-section, and a groove at the base of the cone due to the locally enhanced sputter yield by ions reflected from the cones walls.

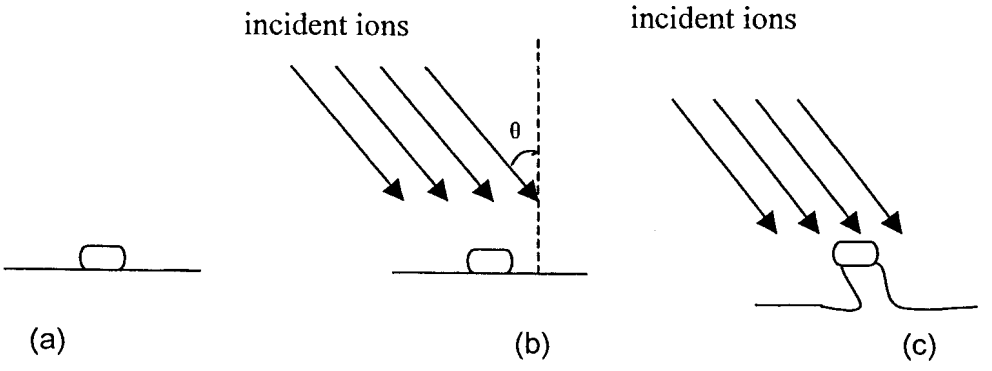

Fig.3.1 A schematic figure showing cone formation as was explained by the impurity-seeding model: (a) sample surface with an impurity atom with lower sputter yield than the original surface. (b) sample bombarded with energetic ions making an angle θ to the sample normal. (c) the faster erosion of the original surface and the impurity atom shielding the surface below it.

Radiation induced topography on semiconductor surfaces cannot be explained by the above-mentioned model due to the high purity and the crystalline nature of semiconductors. Wehner suggested that the seeding material might not have a lower sputter yield, but must have a higher melting point [Weh 85]. Wehner also suggested that seeded cones are a result of the interplay of whisker growth, surface atoms movement and the effects of the sputtering.

(b) Differential sputter model

Sputter yield varies with the angle of incidence of the ions (maximum 60^{o}-80^{o}) and several other effects like spatial distribution of energy deposition function, crystal orientation, and grain boundary defects (pre-bombardment and bombardment induced dislocations). Surface topographical features can be enhanced or deformed by sputter etching. Sigmund's sputter induced topography model suggested that the rate at which the material is sputtered from a point is proportional to the energy deposited at that point [Sig 73]. Carter and co-workers developed a model to explain the development of surface topography [Car 84]. Their model explained some of the surface contours using variations of the sputter yield with ions incidence angle and the spatial variations of ion areic dose. The differential erosional theories had some success in predicting the radiation-induced topography, but not all surface features can be described by these theories.

For InP it is known that phosphorus is preferentially sputtered from the surfaces leaving In enriched surfaces.

(c) Crystallographic Orientation Dependent Model

Palmer and co-workers argued that in polycrystalline material, channelling is a major cause of topographical development [Pal 90], [Pal 92]. This means that the ions penetrate deeply into the lattice and thus do not contribute to the removal of material from the surface if they are incident within critical angles along rows or between planes of densely packed atoms. However, as a result of the ion bombardment amorphization of semiconductor single crystal surfaces even for low ion energy and areic doses, this model is not applicable.

(d)Surface migration model

This model assumes that impurity atoms diffuse across the surface in clusters of ad-atoms, which can cause the appearance of impurity seed cones on the surfaces [Ros 82]. Rossnagel and Robinson proposed that seeding impurity atoms travel across the surface by surface-diffusion and then gather into local clusters initiating the formation of conical structures [Ros 82].

i17585028
b16513290

3.2.2 Growth theories

(a)The re-deposition model

This model, as was reviewed by Malherbe [Mal 94b], proposed that the impurities on the sample, in the ion beam or in the residential gas, initiate cone formation. The cones develop further by re-deposition by the sputtered material and the effect of the local differences in ion deflections.

Despite the fact that there is experimental evidence that re-deposition affects the cone shape [Auc 81], other opinions showed that it only plays a minor role in the development of the sputter cone [Car 83]& [Wil 84]. Sometimes (normal incidence) it even broadens the cone and makes a minor contribution in the longitudinal growth of the cones.

(b) Whisker Growth Model

Wehner proposed that ion irradiation results in the growth of whiskers in certain target surfaces. In his model it was proposed that seed cones are a result of whisker growth, surface diffusion, and the erosional effects of sputtering [Weh 85].
The findings of Floro *et. al.* [Flo 83], that impurity seeding inhibits whisker formation, contradicted Wehner's proposal. The problem with the whisker growth model is that it lacks explanation of the growth mechanisms.

3.2.3 Combined theories

(a) Microregion Model

Gries and Miethe [Gri 87] and Gries [Gri 89], proposed the micro-region model to explain the experimental findings of sputter cone formation on InP. This model presumes that ion bombardment produces an ensemble of micro-crystallite and non-crystalline aggregations of atoms on the InP substrates. The majority of the crystalline micro regions are so small that the interstitials created in collision events between the bombarding and the substrate atoms can then reach an interfacial boundary rather than recombine with a bombardment-induced vacancy. The atoms are then transported to special growth points on the crystalline regions of the surface, where the stubs proceed to grow. These special growth points are postulated to be either screw or Bauser dislocations [Bau 82] either on a surface crystallite of the target material or on a faulted island.

This model also says that ion bombardment-induced compressive stresses favour diffusion towards the surface, and that the crystal growth proceeds until the damage and the sputter rate overtake the growth rate. In the study done by Malherbe *et. al.* [Mal 94a] using transmission electron microscopy (TEM) it was reported that the bombarded surface consists of crystalline and non- crystalline regions in agreement with the model. The other observation was that the cones were found to grow where the InP was not amorphous. It was also found that the vast majority of the cones had the same orientation as the substrate.

(b) Ripple Model

Bradley and Harper [Bra 88] used the mechanisms of surface roughening proposed by Sigmund [Sig 73] and surface diffusion to explain the ripple formation of some semiconductors after ion sputtering (discussed in more detail in 3.3). The theory predicts that for incident ion angles close to the normal of the surface, the ripple wave vector is parallel to the surface component of the beam direction, and the ripple orientation is rotated by 90° for angles close to grazing angles. The ripple wavelengths also depend on the bombarded substrate temperature. This ripple model also shows that the mechanism of surface microroughening leads to instability of plane surfaces against periodic structures. It was assumed that at sufficiently high temperatures and low fluxes, thermally activated surface diffusion dominates ion bombardment induced diffusion (see 3.3). Carter *et. al.* [Car 77] identified two sources of periodic structures; one is the ordered dislocation array that usually occur in ion-irradiated crystalline substrates, and the other is the overlapping of high areal densities, large individual etch pits, which leads to terraced structured formation. Carter's calculations gave the same results as Bradley and Harper's, except a factor of one half difference in the wave vector.

3.3 An overview of some important quantitative theories and models

It is known that the evolution of surface morphology during ion bombardment (deposition or sputtering of the surface) is a result of two competing processes; Erosion and growth of surface features. Stochastic addition or removal of material tends to roughen the surface, while transport driven by surface energy minimization

via processes like surface and bulk diffusion (primary smoothing mechanism for crystalline surface) and viscous flow (dominant for amorphous surfaces) tends to smooth the surface [Mal 94b].

Due to the complexity of the ion-solid interaction there are more qualitative than quantitative models. Studies of bombardment-induced topography of semiconductors have two phases: -

1- The first phase is the explanation of the stochastically rough surfaces and the irregular feature such as cones, pyramids, needle-like structures, and sputter depth resolution.

2- The second phase is investigating regular features such as microscopic ripple-like structures.

The first theoretical model to explain the first phase (the irregular features), was developed by Carter *et. al.* [Nob 69]. They introduced an equation to describe the time evolution of the local height (h) in terms of the ion areic dose rate (J)(ions/cm^2. s), the sputter yield (Y)as function of the angle of incidence (θ) and the ion energy (E) and the atomic density (N):

$$\frac{\partial h}{\partial t} = -\frac{JY(\theta, E)}{N} \qquad (1)$$

The second model was proposed by Sigmund who considered the effect of the spatial dependence of the bombarding ion energy deposition together with the curvature dependent sputter yield [Sig 73]. A more detailed discussion is given in chapter 5 of [Car 84].

The Sequential Layer Sputter (SLS) Model developed by Hofmann [Hof 76], from an earlier approach by Benninghoven [Ben 71], was successful in linking the development of the surface roughness on atomic scale with the stochastic sputtering process. This model predicts continuing roughening of the bombarded surface proportional to the square root of the areic dose (i.e $\Phi^{1/2}$).

Erlewein and Hofmann [Erl 80] were the first to introduce atomic transport into a quantitative topography theory. They used the above-mentioned stochastic sputtering model, in addition to the horizontal surface diffusion resulting in atomic transport into surface vacancies, leading to a smoothing effect of the rough surfaces.

In practice, a smooth topography is not always seen because of the so-called Schwoebel barrier effect. The Schwoebel barrier was first introduced in the late 1960's [Sch 69]. It was proposed to describe growth instabilities in deposition experiments [Vil 91]. It is a potential barrier, which resists step down diffusion of deposited atoms. As a result it increases the probability of the nucleation of the upper level islands compared to lower level islands. Due to the presence of a large number of ad-atoms on sputtered surface during ion bombardment, it is observed that the ad-atoms nucleate in the same way as the deposited atoms. The ad-atoms that reach a step-edge feel the Schwoebel barrier, limiting the interlayer mass transport, thus producing an uphill ad-atom current that leads to an increase of the local slope of the interface, i.e. to a surface instability [Rus 98].

If the Schwoebel barrier is low or the substrate temperature is high enough, then this interlayer transport is efficient (i.e. etch pit deepening is inhibited). The Schwoebel barrier was described as a biased diffusion process [Vil 91], and is used as such in bombardment induced topography theories. The inhibition effect of the Schwoebel barrier is an important factor in the above-mentioned theories but it is very difficult to model in an analytical formulation [Mal 02]. Recently a number of research groups proposed models using the Schwoebel barrier with a reasonable success [Rus 98], [Cos 01].

An early simple quantitative model, based on the work done by Carter [Car 77] was proposed by Hadju *et. al.* [Had 90].This model is based on the elastic instability of the implanted layer when a critical value of lateral stress is reached during ion implantation. This model predicted that for low energy ion bombardment (implantation), the ripple wavelength could be related to the energy of the beam by $\lambda \propto E^{1/2}$. The model had some success in explaining some experimental findings and it also explained the experimental evidence that a minimum areic dose is required before the appearance of ripples. However, it fails to explain several other experimental findings such as the areic dose dependence of the ripple wavelength beyond a minimum value) and the angle of incidence dependence.

Bradley-Harper (B-H) theory was a major advance in the explanation of regular features, like ripples [Bra 88]. It is usually the reference against which the experimental findings are tested. B-H theory determined the curvature dependent sputter yield using a notation belonging to Mullins [Mul 59] i.e. the initial surface W (x, y, 0) lies in the z=0 plane.

Sigmund proposed that the rate at which the material is sputtered away from the surface on an arbitrary point z= h (x, y) is proportional to the energy deposited there by the random slowing down of ions. The Bradley-Harper theory describes the rate at which the material is sputtered away from the surface in two factors. Applying Sigmund approximations [Sig 69], [Sig 73] to equation (1) it becomes:

$$-\frac{\partial h}{\partial t} = \nu_0(\theta,E) - \frac{\partial \nu_o(\theta,E)}{\partial \theta}\frac{\partial h}{\partial x} - \frac{JaY(\theta,E)}{N}\left(\Gamma_1(\theta)\frac{\partial^2 h}{\partial x^2} + \Gamma_2(\theta)\frac{\partial^2 h}{\partial y^2}\right) \qquad (2)$$

where, $\nu_0(\theta,E) = \frac{JY}{N}$ is the erosion rate of the unperturbed planer surface, a is the average depth of energy deposition and Γ_1 and Γ_2 are functions of the ion incidence angle. Periodic perturbations with the smallest wavelength will grow most rapidly in this model.

The other effect used in the B-H theory is the surface diffusion, which leads to smoothing of the surface resulting in an extension of (2) to;

$$-\frac{\partial h}{\partial t} = \nu_0(\theta,E) - \frac{\partial \nu_o(\theta,E)}{\partial \theta}\frac{\partial h}{\partial x} - \frac{JaY(\theta,E)}{N}\left(\Gamma_1(\theta)\frac{\partial^2 h}{\partial x^2} + \Gamma_2(\theta)\frac{\partial^2 h}{\partial y^2}\right) + B\nabla^2\left(\nabla^2 h\right) \qquad (3)$$

For most reported results the ripple orientation agreed with the B-H theory of being perpendicular to the ion beam projection on the surface (see experimental results Chapter 2).

For high temperatures and low dose density rate, if the surface diffusion is thermally activated, the coefficient B is given by:

$$B = D_s \gamma \nu / n^2 k_b T \qquad (4)$$

where, D_s is the surface self diffusivity, γ is the surface free energy per unit area, and ν is the areal density of diffusing atoms.

The average wavelength for the ripples according to Bradley-Harper theory is given by:

$$\lambda \sim (JT)^{\frac{1}{2}} \exp(-\varepsilon_s / kT) \qquad (5)$$

where ε_s is the activation energy for the surface diffusion.

From equation (5), it is shown that the wavelength according to the B-H theory is independent of the areic dose Φ (ions/cm^2).

A number of experimental results disagreed with the B-H theory. For example, the B-H theory predicts an unlimited exponential increase in the ripples amplitude in contrast with the observed amplitude saturation. Similarly, it cannot account for surface roughening, or for ripple orientations different from those defined by the incoming ion direction or parallel to it [Mak 02]. Finally, some experimental results [Mac 92], [Umb 99] showed ripples whose wavelength is independent of temperature (for high temperatures) and linear in the ion energy in contrast with the B-H predictions of ripple wavelength which depends exponentially on temperature and decrease with ion energy.

Several authors extended the Bradley-Harper theory to include viscous flow relaxation, non linear terms to account for higher order variation of sputter yield, interlayer diffusion, crystallographic dependence of surface and bulk diffusion, the random arrival of ions and the statistical variations of the sputter rate and a smoothing term to account the effect of the recoiling-adatom diffusion induced by ion irradiation, resulting in the Kuramoto-Sivashinsky (KS) partial differential equation. The KS equation is a non-linear equation that describes the time evolution of the local-surface height and can be written in the generalized form [Car 99]:

$$\frac{\partial h}{\partial t} = -\rho\left(\left|\frac{\partial h}{\partial x}\right| + \left|\frac{\partial h}{\partial y}\right|\right) + \sum_m \left[A_m\left(\frac{\partial h}{\partial x}\right)^m + B_m\left(\frac{\partial h}{\partial y}\right)^m\right] + \sum_2^4 \left[C_n \frac{\partial^n h}{\partial x^n} + D_n \frac{\partial^n h}{\partial y^n}\right] + \eta(x,y,z) \qquad (7)$$

In equation (7) the first term on the right hand side represents viscous relaxation. The first summation term shows that sputtering causes erosion along the local surface normal with a rate dependent on the trigonometric function of the surface gradients [Sig 69]. The second summation indicates the effects of the surface curvature-dependent sputter rate (n=2), surface (n=4) and bulk (n=3) diffusion, and the final term represent the noise. It is not easy to make a generalized conclusion from equation (7) because of the effect of the non-linear terms.

Rudy and Smirnov [Smi 96] used a different approach, when they explained the ripples using a hydrodynamic model. The amorphized layer, due to ion bombardment, is considered as a Newtonian fluid on a hard surface in the field of external force. The movement of the amorphous layer is then considered in terms of continuity equations for an incompressible fluid and also is formulated as a boundary

value for the Navier- Stokes equation. Their equation agreed well with the experiment they did with N_2^+ on Si substrates.

3.4 Conclusion

In this chapter a brief review of the major theories and models developed to explain the morphological properties of surfaces eroded by ion bombardment is given.
A general review of the different groups of theoretical models is given and some of the quantitative theories and models were discussed.

The major theoretical explanations of this phenomenon started with the continuum theory by Sigmund [Sig 96], [Sig 73]. The early explanation was by Bradley and Harper, who attributed the processes to the competition between the curvature dependent sputter rate, which leads to roughening, and thermal diffusion, which leads to smoothing. A number of theories were developed to add this effect, which the B-H theory neglected. One of the most important attempts is the work done by Carter [Car 99].

As a conclusion one could say that the evolution of solid surface topography during ion bombardment is governed by the interplay and competition between the dynamics for surface roughening on one hand, and the material transport in surface diffusion. The removal of atoms during sputtering roughens the surface because of the curvature dependence of the sputter yield [Bra 88], which is described by the so-called negative surface tension. Surface diffusion is driven by the minimization of the surface Gibbs free energy and acts like a positive surface tension. These processes compete during ion beam erosion and are responsible for the creation of characteristic surface patterns [Hab 99].

References: Chapter 3

[Auc 81] O. Auciello and R. Kelly, *Nucl. Instrum. Meth. Phys. Res.* 182/183 (1981) 267.

[Bau 82] E. Bauser and H.Strunk, *Thin Solid Films* 93 (1982) 185.

[Ben 71] A. Benninghoven, *Z Phys.* 230 (1971) 403.

[Bra 88] R. M. Bradley and J. M. E. Harper, *J. Vac. Sci. Technol.* A 6 (1988) 2390.

[Car 77] G. Carter and M. J. Nobes, F. Paton, J.S. Williams and J.L. Whitton, *Radiat. Effects* 33 (1977) 65.

[Car 83] G. Carter, B. Navinsek and J.L. Whitton, in *Sputtering by particle bombardment II*, R. Behrish (Ed.), Springer-Verlag, Berlin (1983) 640.

[Car 84] G. Carter and M. J. Nobes, in *Ion Bombardment Modification of surfaces*, O. Auciello and R. Kelly (Ed.), Elsevier, Amsterdam, (1984) 163.

[Car 99] G. Carter, *Phys. Rev.* B 59 (1999) 1669.

[Cos 01] G. Costantini, S. Rusponi, F. Buatier de Mongeot, C. Boragno and U. Valbusa, *J. Phys. Condens. Mat.* 13 (2001) 5875.

[Erl 80] J. Erlewein and S. Hofmann, *Thin Solid Films* 69 (1980) L39.

[Flo 83] J. A. Floro, S. M. Rossnagel and R. S. Robinson, *J. Vac. Sci. Technol.* A 1 (1983) 1398.

[Gri 87] W. H. Gries and K. Miethe, *Microchim. Acta.* 1(1987) 169.

[Gri 89] W. H. Gries, *Surf. Interface Anal.* 14 (1989) 611.

[Hab 99] S. Habenicht, W. Bolse, K. P. Lieb, K. Reimann and U. Geyer, *Phys. Rev. B* 60 (1999) R 2200.

[had 90] C. Hadju, F. Paszti, I. Lovas and M. Fried, *Phys. Rev.* B 41 (1990) 3920.

[Hof 76] S. Hofmann, *Appl. Phys.* 9 (1976) 59.

[Mac 92] S. W. MacLaren, J. E. Baker, N. L. Finnegan and C. M. Loxton, *J. Vac. Sci. Technol.* A 10 (1992) 468.

[Mak 02] M. A. Makeev, R. Cuerno and A.- L. Barabasi, *Nucl. Instrum. Meth. Phys. Res.* B 197 (2002) 185.

[Mal 94a] J. B. Malherbe and N. G. van der Berg, *Surf. Interface Anal.* 22 (1994) 538.

[Mal 94b] J. B. Malherbe, CRC *Crit. Rev. Solid State Mat. Sci.* , 19 (1994) 129.

[Mal 02] J. B. Malherbe, in *Ion Beam Analysis of Surfaces and Interfaces of Condensed Matter Systems*, P. Chakraborty (Ed.), Nova Sciences Publ, New York (2002) Chapter 11.

[Mul 59] W. W. Mullins, *J. Appl. Phys.* 30 (1959) 77.

[Nob 69] M. J. Nobes, J. S. Colligon and G. Carter, *J. Mater. Sci.* 4 (1969)730.

[Rus 98] S. Rusponi, G. Costantini, C. Boragno and U. Valbusa, *Phys. Rev. Lett.* 81 (1998) 4184.

[Pal 90] W. Palmer, K. Wangemann, S. Kampermann and W. Hosler, *Nucl. Instrum. Meth. Phys. Res.* B 51(1990) 34.

[Pal 92] W. Palmer and K. Wangemann, *Surf. Interface Anal.* 18 (1992) 52.

[Ros 82] S. M. Rossnagel and R. S. Robinson, *J. Vac. Sci Technol.* 20 (1982) 195.

[Sch 69] L. Schwoebel, *J. Appl. Phys.* 40 (1969) 614.

[Sig 73] P. Sigmund, *J Mater. Sci.* 8 (1973) 1545.

[Smi 96] V. K. Smirnov, S. G. Simakin, E. V. Potapov and V. V. Makarov. *Surf. Interface Anal.* 24 (1996) 469.

[Umb 99] C. C. Umbach, R. L. Headrick, B. H. Cooper, J. M. Balkely and E. Chason, *Bull. Am. Phys. Soc.* 44 (1) (1999) 706.

[Vil 91] J. Villan, *J. Phys.* I (France) 1 (1991) 19; I. Elkainani et al., *J. Phys. I* (France) 4 (1994) 949.

[Weh 85] G. K. Wehner, *J. Vac. Sci. Technol.* A 3 (4) (1985) 1821.

[Wil 84] I. H. Wilson, J.Belson and O. Auciello, , in *Ion Bombardment Modification of surfaces*, O. Auciello and R. Kelly (Ed.), Elsevier, Amsterdam, (1984) 225.

Chapter 4

Experimental Set-up

4.1 InP Sample Preparation

Factory-polished InP (100) samples n-doped with S to 4 x 10^{18} atoms/cm^3, were cleaved in air to the size of ~ 2 x 3 mm for each sample. Prior to introduction into the vacuum chamber, the samples were rinsed in isopropyl alcohol and dried. Powdery InP particles on the sample surface, resulting from the cleaving, were removed using a soft brush.

The samples were accurately cut to the plane and that was confirmed by the measurements done on AFM images for unbombarded InP wafers surfaces.

Maximum care had been taken in mounting the samples, so that the ion beam could be positioned at the centre of the sample away from the clamp (which secures the sample) to avoid the seeding cone development. This is the phenomena described by Wehner [Weh 85], which gives rise to cone formation on ion bombarded surfaces as a result of foreign atoms that may be present as impurity atoms in the target surface or be supplied during sputtering from another source (e. g. the clamp).

The ion bombardment was done under ultra high vacuum conditions (UHV) in an Auger electron spectroscope (AES) system using a Physical Electronics (04-303A) differentially pumped ion gun. The sputtering was done in the raster mode (2mm x 2mm square rastered) to avoid crater edge effects [Mal 81]. The samples were bombarded with 5 keV N_2^+ ions with areic doses of 1 x 10^{14}, 5 x 10^{14}, 1x10^{15}, 5x10^{15}, 1x10^{16}, 5x10^{16}, 1x10^{17} and 5x10^{17} ions/cm^2. For Φ = 1 x 10^{14}, 5 x 10^{14}, 1x10^{15} and 5x10^{15} ions/cm^2 an ion areic dose rate of 1.6 x 10^{12} ions/cm^2 s was used. For Φ = 1x10^{16} and 5x10^{16} the areic dose rate was 3.6 x 10^{13} ions/cm^{2}s. For the doses Φ = 1x10^{17} and 5x10^{17} ions/cm^2 the ion areic dose rate was 1.8 x 10^{14} ions/cm^2 s. No

mass separation of N_2^+ and N^+ was done during sputtering. The well-known cracking pattern of molecular nitrogen (N_2^+/N^+) ratio of ~10) indicates that the nitrogen impinging the surface is mostly N_2^+ [Tan 90]. The pressure in the main chamber, before starting the bombardment was about 1 x 10^{-9} Torr and was kept at ~ 10^{-8} Torr during the sputtering by running the turbo pump connected to the main chamber throughout the experiment.

The angle of incidence was kept at 41^o to the sample normal which is approximately the angle reported to give the highest roughness for InP after noble gas ion bombardment [Dem 96]& [Pan 98]. The ion current was measured using a Faraday cup. The areic dose Φ was calculated using the equation;

$$\Phi = \frac{I_i \times t}{e\ A\cos\theta_i}$$

where,

I_i is the ion current

t is the sputtering time

A area of the hole of the Faraday cup

θ_i the angle between the ion beam and the sample normal

e electron charge

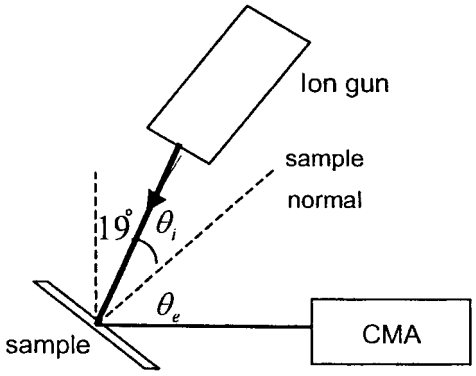

Fig.4.1 A schematic illustration of the geometry of CMA and the ion gun with respect to the normal of the sample. θ_i is the angle between the ion beam and the sample normal and θ_e is the angle between CMA and the normal.

The experiment was done on three sets of samples under similar conditions, to test the reproducibility of the results.

4.2 Scanning Electron Microscopy

4.2.1 Introduction

M. von Ardnee constructed the first scanning electron microscope in 1938, and although it developed through the years, the essential features stayed the same. The basic components of the SEM are the electron gun, lens system, deflection systems, cathode ray tubes for viewing, and the electronics associated with them.
Scanning electron microscopy is one type of microscopy that relies on the atomic properties of the material to explore the surface topography. Interaction between the incident electron beam and samples in the SEM produces a spectrum of electrons with different energies varying from zero up to that of the incident beam. The distribution of the energies of the electrons produced in this process is generally divided into two different groups, backscattered electrons having energies comparable to that of the incident electrons and secondary electrons with energies typically of few tens of electron volts (0 – 50 eV).

Back-scattered electrons and secondary electron are both used in the SEM for imaging purposes. The backscattered signal is the result of high angle elastic scattering events, while the secondary signal is the result of knock-on inelastic collisions. In both cases the physics of interaction between the incident beam and the sample determine the important properties of the images such as the optical resolution and the image contrast [Joy 84].

In order to produce contrast in the image, the signal intensity from the beam specimen interaction must be measured from point to point across the specimen surface. The function of the deflection systems is to scan the beam along a line and then displace the line position for the next scan so that a rectangular raster is generated on both the specimen and the viewing screen. Two pairs of electromagnetic deflection coils (scan coils) are used to control the raster of the beam. The image is constructed in the cathode ray tube (CRT) scanned in synchronism with the scan of the electron beam over the specimen, controlled by the same scan generator. The signal derived from one of the detectors is amplified and used to control the brightness of the CRT (intensity modulation), often with some form of processing applied to enhance the visibility of the features of interest.

The magnification M of the specimen is the ratio of the linear size of the viewing screen, known as the cathode ray tube (CRT), to the linear size of the raster on the specimen. Thus, increasing the magnification may be obtained by exciting the scan coils less strongly so that the beam deflects smaller distance on the specimen [Gol 92]. The samples in the sample holder for the SEM are grounded to avoid charging effects from the electron beam.

SEM could be operated in several operational modes. The two most common are the back-scattered electrons imaging (BSI) and the secondary electrons imaging (SEI). For BSI on most specimens at medium and high energies of the incident electron beam, the yield of the backscattered electrons is much higher than that of the secondary electrons. Several operational modes such as electron channelling and

atomic number contrast are restricted to the backscattered mode. The other type of electrons that one can use for imaging is the secondary electrons.

4.2.2 Secondary Electrons Imaging (SEI)

The SEI mode in the SEM is widely used because its signal includes a wide variety of information and the ease and efficiency of collecting the secondary electrons.
Most of the secondary electrons detected in SEM are the valence electrons that are dislodged from atoms in the outer 0 - 10 nm of the specimen surface by the incident electron beam. The number of the secondary electrons generated at a given point at a fixed beam current and energy depends basically on the angle at which the beam strikes the specimen surface at that point. More electrons are emitted when the surface is inclined to the beam than when the surface is perpendicular to it as a result of the increasing of the electron path length (volume of interaction) near the surface. Consequently, image contrast changes as the beam moves over the surface in a manner related to the topography of the specimen surface.

The main disadvantage of using the SEI in the conventional SEM is that the images are poorly characterized, i.e. electrons collected by the detector come from different sources - see fig. 4.2(a). Only the signal from the secondary electrons produced directly by the incident beam at the position of the electron beam on the sample carries information about the sample, the other electrons only contribute to the background intensity and the statistical noise in the images.

4.2.3 Field Emission in-lens Scanning Electron Microscope (FE-SEM)

The field emission cathode in the electron gun of the scanning electron microscope provides a narrower probing beam at low as well as high electron energies, resulting in improvement in the spatial resolution.

The greatest advantages of the cold field emission gun are that [Gol 92]: -

1) The virtual source is so small that only simple optics is required to produce a probe of a nanometre size, whereas the brightness is very high, and
2) The energy spread is very low, which improves performance for low voltage operations.

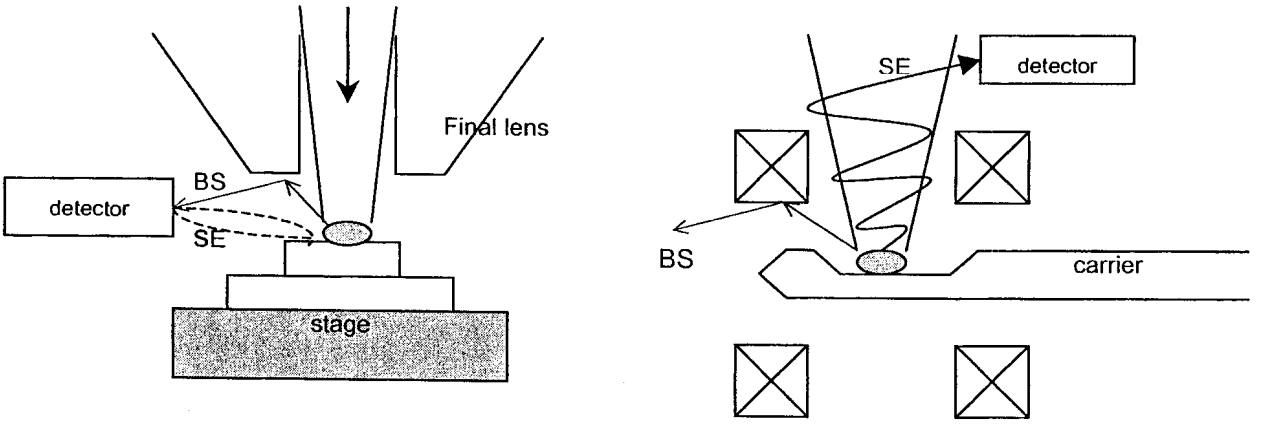

(a) conventional SEM (b) in-lens FE-SEM

Fig.4.2 A schematic showing the mechanism that provides the resolution advantage of the immersion lens FE-SEM.

Figure 4.2(a) shows that in conventional SEM, the secondary electron detector is close to the sample. In addition to the secondary electrons from the sample, the secondary electrons from the walls produced by high-energy back-scattered electrons also contribute to the overall secondary electron signal. By reducing the contribution of the secondary electrons produced by this backscattering in the total SE image, it is possible to obtain sharper images. For the in-lens FE-SEM as schematically shown in figure 4.2(b), the sample sits in the field of the objective lens. By doing this the low energy secondary electrons, which are desired to be detected, are trapped by the field of the lens and travel up the column to the upper detector reducing the contribution of BS and BS-produced secondary electrons in the image.

In this study a JEOL 6000F (cold field emission in lens scanning electron microscope) in (SEI) mode with a resolution of 0.6 nm at 30kV (manufacturer's specifications) accelerating voltage was used to investigate the topography of InP before and after ion bombardment. The accelerating voltage used was 5 kV and the samples were looked at when the incident electron beam was parallel to or made 30^o or 60^o to the sample normal, with magnifications 10,000, 25,000 and 50,000. The information obtained gave a general idea about the shapes, size and distribution of the sputtered cones and the ripple - like structures. The term cone (or sputter cone) is a general term used to describe the cone-like features that appear on the bombarded surface.

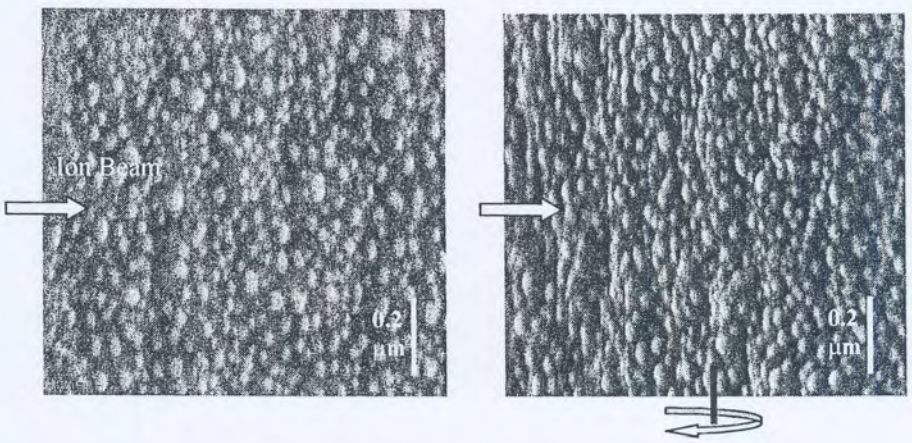

(a) *(b)*

Fig. 4.3 FE-SEM images of nitrogen bombarded InP to the areic dose $5x10^{17}$ ions/cm^2 : (a) electron beam perpendicular to the sample, (b) sample tilted 30^o to the electron beam. (Fig (a) and (b) are not from precisely the same area)

Figure 4.3(a) shows a typical FE-SEM image with an original magnification of 50,000. The highest parts (cones with inclined sides) of the surface appear brighter than the lower parts as a result of the higher intensity of the secondary electrons emitted from the cone-like features. Figure 4.3(a) can be used to calculate the density and distribution of the cones. Tilting the sample fig. 4.3(b) allows clearer viewing of the regularity of the surface features' shapes. Calculations can be done to roughly determine the depth of field and dimensions of the cones with the knowledge of the tilt angle.

4.3 Atomic Force Microscopy

4.3.1 Introduction and a brief background

Gerd Binnig and Heinrich Rohrer shared the Nobel prize in physics in 1986 for inventing the scanning tunnelling microscope (STM), which they developed in 1981. The STM allows imaging of solid surfaces using the so-called tunnelling current between the substrate and a sharp tip, which is scanned across the surface. Thus it can only work for conducting materials.

The success of STM opened the door to the invention of other scanning probe microscopes, which all have the same principle concept of mechanically scanning a sharp tip over a sample surface. In 1986 Binning and his co-workers [Bin 86] investigated the forces between single atoms and to their surprise, it was found it is easy to make a cantilever with a spring constant weaker than the equivalent spring constant between the atoms. This allows a sharp tip to image both conducting and non-conducting samples at atomic resolution [Rug 90].

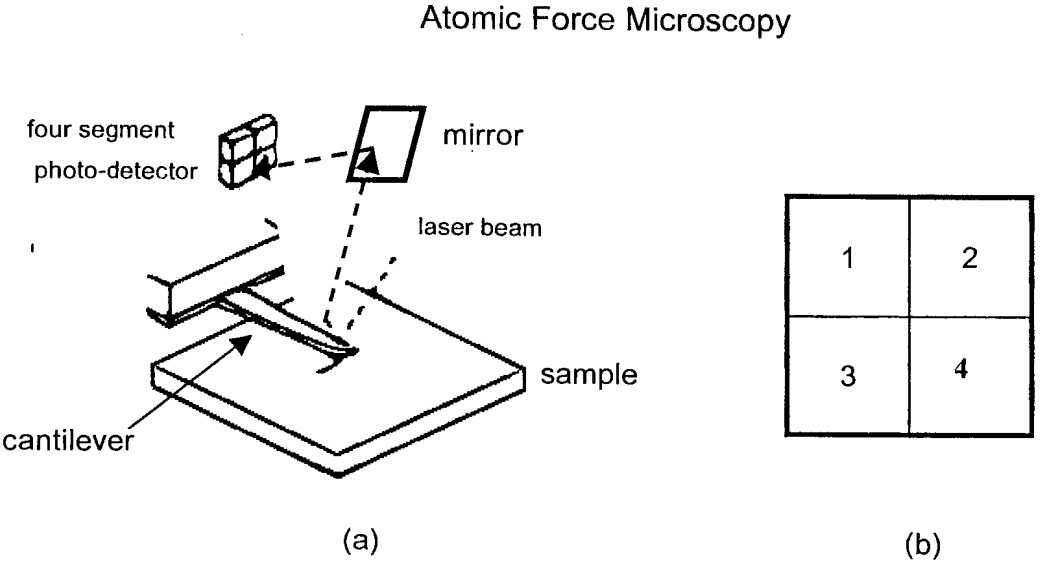

Fig. 4.4 A schematic diagram showing the Atomic Force Microscope; (a) An illustration of some of the essential components of the AFM used in this study. (b) Numbering (see text) of the segmented photo-detector.

Atomic force microscopy usually consist of five main components (see fig. 4.4)

(1) A sharp tip mounted on a flexible cantilever.

(2) A way of sensing cantilever deflection. In the AFM used in this study (as illustrated in fig. 4.4) the reflection of a laser beam from the cantilever is used.

(3) A feedback system to monitor and control the cantilever deflection

(4) A mechanical scanning system using piezoelectric crystals. (In our case scanning of the specimen).

(5) A display system that converts the measured data into an image.

The basic objective of the operation of the AFM is to measure the forces (at the atomic level) between a sharp probing tip (which is attached to a cantilever) and the sample surface. As the tip is scanned across the surface, it is deflected as it moves over the surface corrugation. In the AFM used in this study the reflected laser beam falls on a segmented photo-detector. The amount of the cantilever deflection can then be calculated from the difference in the light intensity on the different sectors of the photo-detector.

The up and down (top-bottom) movement of the reflected laser, providing the so-called (T-B) signal, is the basis of the normal AFM images giving the topography of the sample. The T-B signal is given by (s1+s2) - (s3+s4), where (s1) stands for the signal detected from the part numbered 1 of the photodiode and so on (see fig. 4.4 (b)).

A feedback electronic circuit is combined with a probe (sensor and piezoelectric ceramics to create the positioning mechanism. This positioning mechanism acts as a compensation network that monitors the cantilever deflection. By adjusting the height (Z) of the sample (or the cantilever) this positioning mechanism keeps the force between the tip and the sample surface constant.

Lateral Force Microscopy (LFM) (not used in this study), uses the frictional force between the tip and the substrate to construct images. LFM uses the torsional deflection (L-R signal), where L-R = (s1+s3) – (s2+s4) (see fig. 4.4(b)).

4.3.2 Tip-Sample Interaction

AFM image contrast is obtained in different operational modes:

(1) Contact Mode

The most common mode is force microscopy, where, the tip scans the sample in close contact with the surface. By contact we mean in the repulsive regime of the inter-molecular force curve (see fig. 4.5). Despite the fact that contact mode gives good information about the topography of the surface under investigation, it has some disadvantages. One of the main disadvantages of this mode is that there exist large lateral forces on the sample, which as the tip is dragged over the specimen it can, thereby, damage soft samples by a scratching mechanism.

(2) Lateral Force Mode

Differences in surface frictional characteristics can be obtained simultaneously with contact mode imaging. One usage example is to determine the different chemical species on surfaces by their different frictional forces.

(3) Non-contact mode

In this mode the cantilever is oscillated, at its resonant frequency, above the surface of the sample at such a distance that it is no longer in the repulsive regime of the intermolecular curve. The distance should still be small enough for the force (interaction) between the tip and the sample to exist (of the order of a few tens of nanometres). As the probe gets closer to the sample surface, the force gradient will change due to the forces between the tip and the sample. This change in force causes a change in the amplitude and frequency of the oscillation of the probe tip. Both the changes in amplitude and the changes in phase can be detected and used to control the feedback-control loop. The change in the amplitude or/and the frequency of the oscillation is then used to construct an image.

This mode is very difficult to operate in ambient conditions. For example, a thin layer of water contamination on the surface will invariably form a small capillary bridge between the tip and the sample and cause the tip to jump to contact mode.

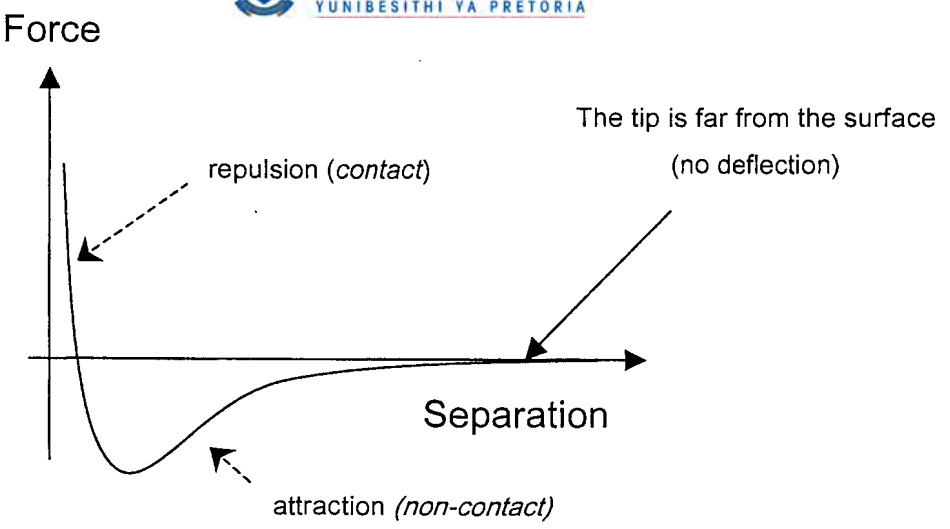

Fig. 4.5 The inter-molecular force curve showing schematically the force as a function of the distance between the tip and the sample.

(4) Tapping Mode

In this mode the tip gently taps the surface while oscillating at the resonance frequency, thus significantly reducing the contact time. Tapping mode is a key advance in AFM imaging, because it effectively eliminates lateral (shear) forces.

In contact AFM, electrostatic and / or surface tension forces from the adsorbed gas layer pull the scanning tip toward the surface. It can damage samples and, thereby, distort image data. Therefore, compared to the non-contact or tapping mode contact, this mode imaging is heavily influenced by frictional and adhesive forces. Non-contact imaging generally provides low resolution and can also be hampered by the contaminant layer, which can interfere with oscillation.

Tapping Mode AFM was developed as a method to achieve high resolution without inducing destructive frictional forces both in air and fluid. With the Tapping Mode technique, very soft and fragile samples can be imaged successfully.

4.3.3 AFM/ Cantilever/ tip specifications

The scanning probe microscope used in the present study was a commercial instrument; model TMX 2000 " Discoverer" (TopoMetrix, CA). The AFM cantilever is fabricated from silicon nitride (Si_3N_4). The cantilever is designed in a "V" shape, with the probe tip integrated onto the underside of the end of the cantilever (see fig. 4.6). The TopoMetrix cantilever used in this investigation has a force constant of 0.032 N/m and a nominal resonance frequency of 17 kHz. The AFM tip is a silicon nitride

pyramid 4 μm base 4 μm high, with an aspect ratio (height to width ratio) ~ 1: 1 and a radius < 50 nm.

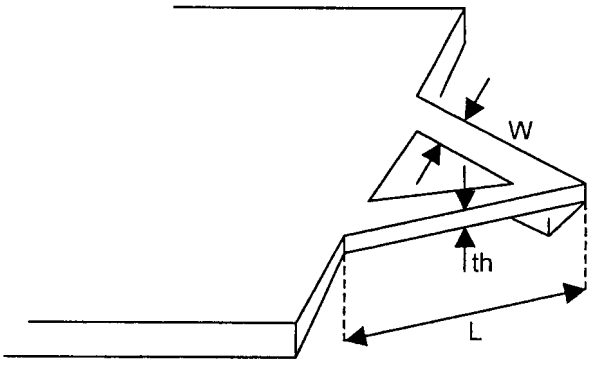

Fig.4.6 A schematic diagram of a V-type Si_3N_4 cantilever. The dimensions for the cantilever are arm length (L) equal to 200μm, thickness th = 0.6 μm and width W =18 μm and a TopoMetrix tip type 1520.

The topography of the InP single crystals before and after nitrogen bombardment was studied by means of AFM in contact mode. All the measurements were done in ambient conditions in constant force mode using a scanner with a maximum scan range of 7x7μm². A video camera system connected to a TV screen was used to determine the position of the tip on the samples. The central part of the sample surfaces was investigated because it was the part of the sample where the ion beam was uniformly reacting with the sample. For some samples a few more areas were investigated e.g. near the clamp; near the edge of the sample and on the un-sputtered parts. The reason for that is to see if the sputtered surface is homogenous and to see the difference between the sputtered and the un-sputtered regions.

Quantitative measurements on the images from the un-sputtered parts were used as reference values. Scan sizes of 7 x 7, 5 x 5, 2 x 2, 1 x 1 and 0.5 x 0.5 μm² were recorded and the resolution (number of pixels) for each image was 200 x 200.

For all the images we started from the same values of the scan parameters (setpoint, scan rate and PID constants with P standing for proportional gain, I for integral gain, and D for derivative gain), P = 6, I = 3 and D = 0.1. The PID feedback sums the output from three separate feedback loops. Proportional gain determines the response time to small features. The integral gain responds to large features. Derivative gain tends to reduce oscillations, but amplifies high frequency noise. In each case final optimisation was performed, to get images with minimum noise. For the same reason a scan rate of (2 x scan range) was used. For example for 5 x 5μm² areas of scan the scanning rate was 10μm/s, which correspond to a scanning

frequency of 2 Hz. The PID settings and the scanning speed determine the response time of the feedback loop to correct for the cantilever deflection.

4.3.4 Image Processing and Analysis

4.3.4.1 Processing

The TopoMetrix software version 3.06.06 was used for image processing. A slope correction to compensate for the tilt of samples relative to the scanning plane in the form of a first order two-dimensional polynomial was applied to the AFM images. This function uses a least squares algorithm to fit the image to a plane and then subtract the plane from the image. 2D levelling levels the data in both the x and y direction. Fig. 4.7(a) shows an AFM image before applying the slope correction. The height difference is ~50 nm and the horizontal line profile shows that the image is tilted. In fig. 4.7(b) the grey scale shows that the height differences in the image were reduced (to ~ 17nm) after applying the slope correction. The line profile 4.7(b) shows that it is possible to observe more of the real structures after levelling the image.

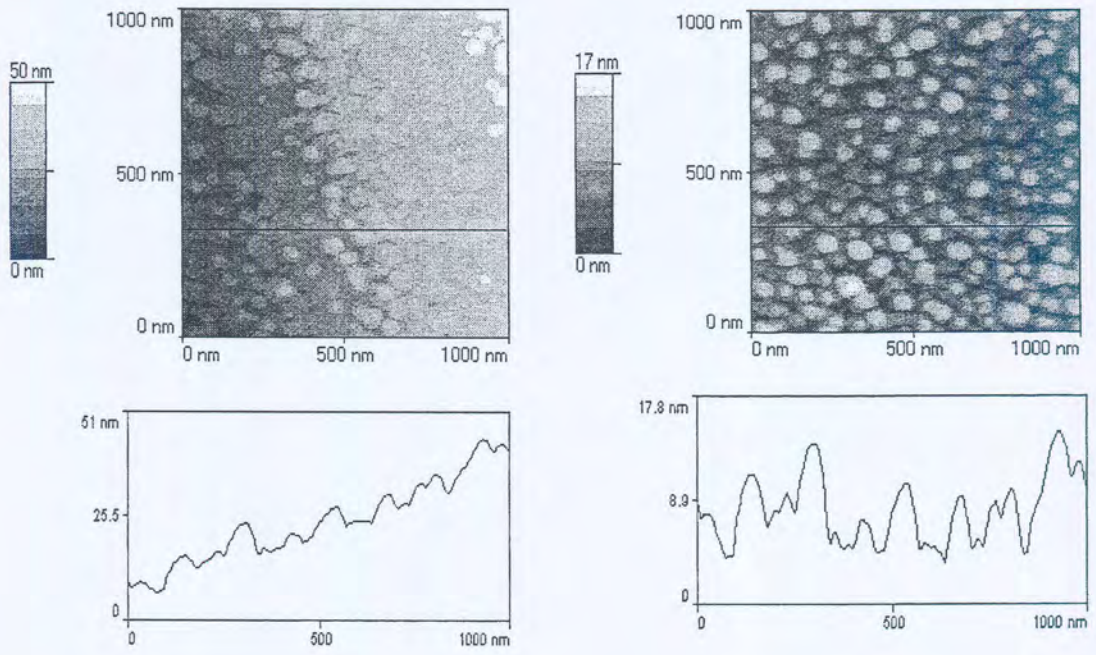

(a) (b)

Fig.4.7 AFM image and the corresponding line profiles in the x direction of a nitrogen bombarded InP surface to an areic dose of 1x10^{16}ions/cm^2 (a) The raw AFM image and the corresponding line profile in the x direction, (b) The levelled AFM image (after applying a first order polynomial in the x-y directions) and the corresponding line profile (for the same line).

Some images were levelled further using a second order polynomial in the x and y direction to compensate for the bowing of the piezoelectric tube. Bow results from the drift of the piezo-scanner particularly in large scan sizes due to the effect of piezoelectric non-linearity, hysteresis and creep [Fan 97].

All the images in figures (fig. 4.7, 4.9, 4.10, 4.11 and 4.12) are the same AFM recording with the projected (onto the surface) direction of the ion beam from left to right.

Three-dimensional representations of the AFM images were also used in this study. The reason for that is to give a better view of the sample and the shapes and heights distribution of the cones over the surfaces (see fig. 4.8).

In this study the SEM images were used for exploring the surfaces of the samples to see if the topography of the surfaces is homogenous and to determine the shapes of the topographical features. The other reason is to see if there is a similarity between the surface morphology determined by FE-SEM and the AFM. However, the main quantitative study was done using the AFM.

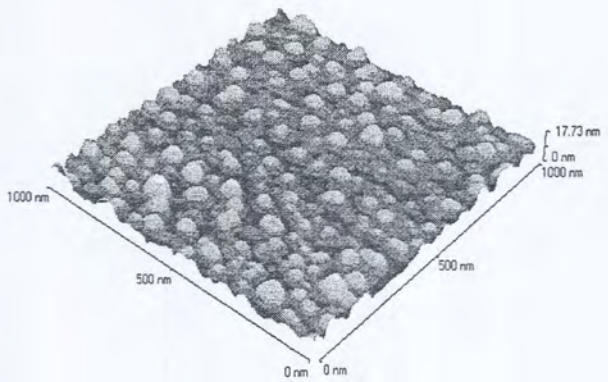

Fig. 4.8 A three-dimensional representation of the same AFM image (fig. 4.7).

4.3.4.2 Quantitative surface roughness/ topography parameters

Most of the studies of semiconductor topographical changes after ion bombardment described the surface development in terms of surface root mean square roughness R_{rms} [Kie 97], [Dem 96], [Liu 03] & [Bar 89].

The root mean square roughness R_{rms} is defined as,

$$R_{rms} = \sqrt{\frac{\sum_{n=1}^{N} \left(Z_n - \overline{Z}\right)^2}{N - 1}}$$

where;

Z_n : Height measurement of pixel n.

$\overline{Z}$: Arithmetic mean height.

N : Total number of pixels (200x200).

The R_{rms} as a statistical measure is used widely to characterize the development of the topographical features under the different bombarding conditions. It is known that the R_{rms} is sensitive only to vertical features and not horizontal ones [Fan 97], [Kie 97]. The R_{rms} value for surfaces with different spatial variations may be identical; hence it does not fully characterize the surface [Spa 94]. It is therefore important to report more roughness parameters besides the root mean square roughness [Dem 95].

A number of studies were done to compare the R_{rms} roughness calculated from AFM images and other techniques. For example, a study was done to compare the R_{rms} calculated from AFM images and images obtained using the grazing incident angle X-ray reflectometer (GIXR) and ellipsometry. All the studies agreed that its value is not an absolute, but it could be used to investigate the trend [Zym 00], [Fan 96] & [Fan 97].

In this work line profiles across the surface were used (see fig.4.9) to measure the average values (calculated using at least five lines and five images) of maximum height of the profiles above the mean line $\left(\overline{Z}\right)$, which could be written as [Top 00];

$$R_p = Z_{\max} - \overline{Z}$$

The other measured value from the line profiles is, R_t, which is the maximum peak to valley height in the profile;

$$R_t = Z_{\max} - Z_{\min}$$

For the AFM image shown in fig. 4.9 the values recorded were, R_p = 7.46 nm and R_t = 10.93 nm.

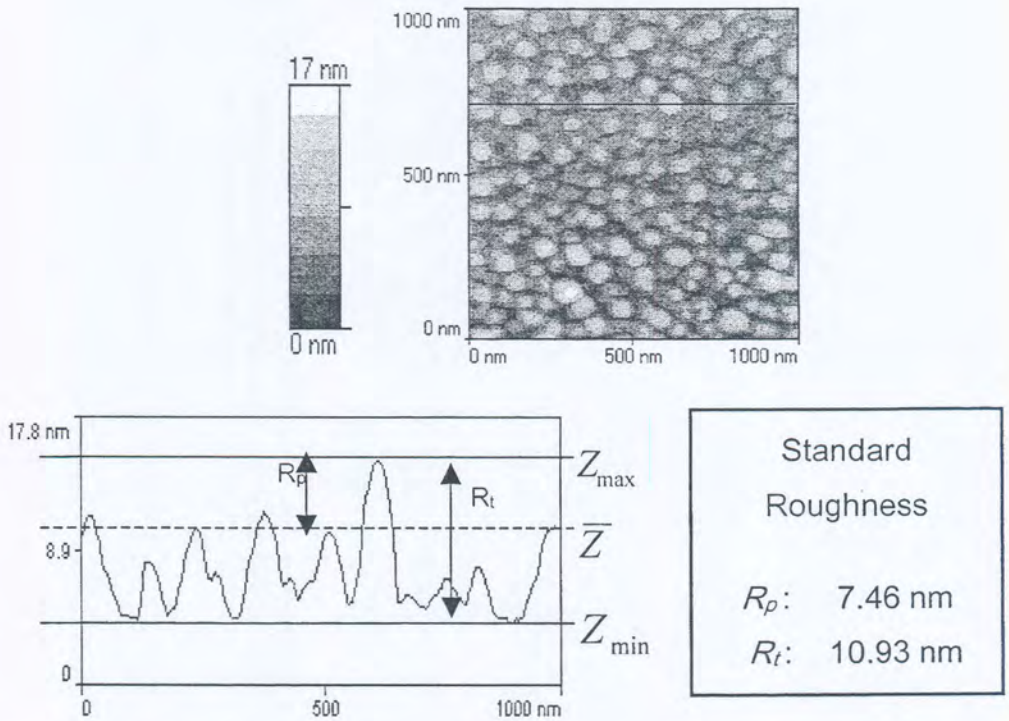

Fig. 4.9 An AFM line profile and the corresponding values for R_p and R_t across the line.

The line profiles could also be used for measuring the size of the features (see fig. 4.10). The sizes of the cones (x-y width and height z) can be calculated from line profiles. From the line it is clear that the line passes at the centre of only one cone, so only this cone could be used for the measurements along that specific line.

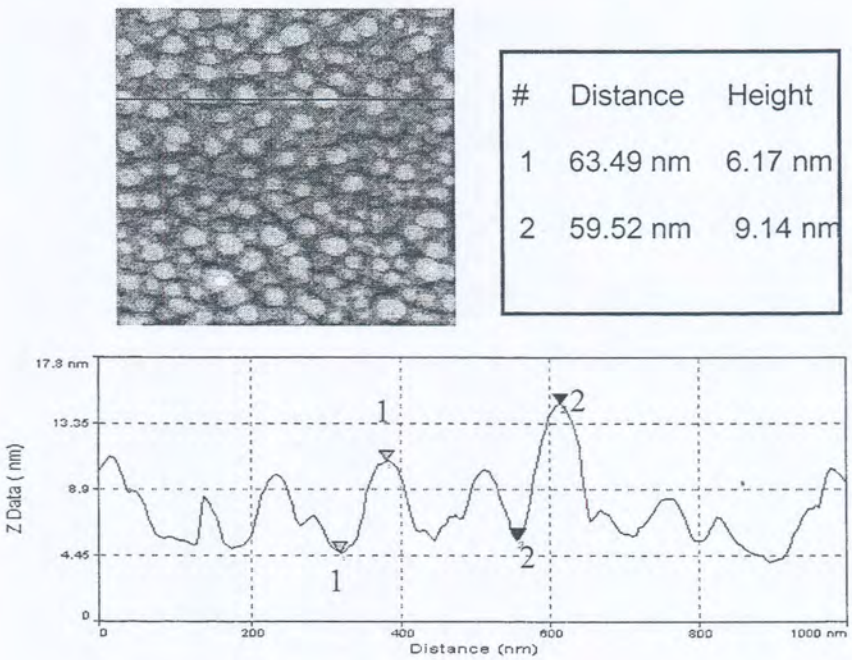

Fig.4.10 Measuring cones heights and dimensions from a line profile.

As was discussed previously, it is important to characterize the surface under investigation by more than one parameter. The roughness factor, defined as the surface (real) area to projected area ratio, is another parameter used in this study (see fig. 4.11).

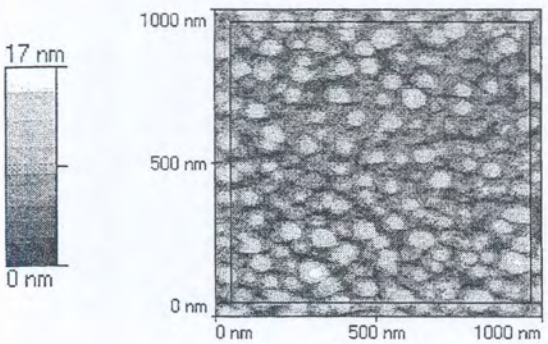

Area R_{rms}	2.2128 nm
Projected area	8.32E+5 nm^2
Surface area	8.57E+5 nm^2

Fig. 4.11 Typical area selected for analysis. For the above image the R_{rms} = 2.2128 nm and the roughness factor = 1.03

Another way of quantifying surface roughness is fractal dimension (*FD*) analysis. The fractal dimension characterizes the surface by only one numerical value. For three-dimensional images, the values lie in the range 2 to 3. Perfectly smooth surfaces have a value of 2, and for a completely rough surface the value is 3. This value can be directly correlated with observed phenomena and it can be used to distinguish between surfaces that other parameters (e.g. R_{rms}) classify as the same [Mal 94]. For a surface profile, there are several ways to determine the surface *FD*. The method used here is called the lake filling method, which involves choosing a height Z, such that approximately half the structures (Z values from the different pixels) on the surface are above the chosen value and the other half are below. The *FD* of the surface can then be determined from the slope of a log-log plot of lake Perimeter vs. Lake Area (see fig. 4.12).

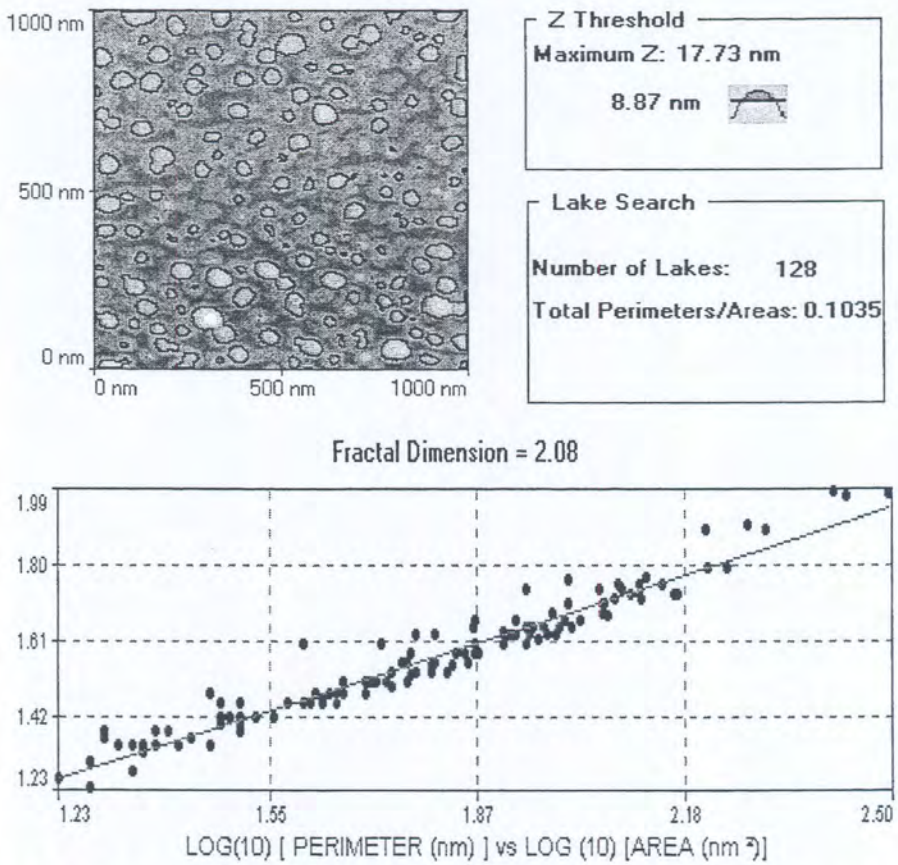

Fig. 4.12 Fractal analysis (FD of the surface = 2.08) and the number of cones is approximately = 128.

General comments

In a study done by Kiely *et. al.* [Kie 97] it was shown that any measure of surface roughness is scale dependent. The roughness was reported to increase with increasing the length over which it was measured. It was also found that there are characteristic (critical) lengths at which the dependence changes. Several factors may explain this phenomenon. The increasing variety of features on the surface with increasing the area over which the measurement is taken, the possibility of presence of ad-atoms and dust particles on the surface and artifacts resulting from the scanner drift for scanning large areas are also possible reasons for that effect.

All the above-mentioned experimental observations made it more convenient to compare images with the same scan range. In this study the scan range 1 x 1μm^2 was used for all the parameters but for the R_{rms} other scan ranges were also used (see fig. 5.16). For the sample with ripples, the surface waviness (wavelength) was measured besides the other roughness factors.

When performing the area analysis for all the images an area smaller (80-90% of original scanned size) than the originally scanned area, indicated by the square in the image (see fig. 4.11) was selected for the measurements. The reason for that is, to avoid image edge effects that are common as a result of the mechanical movement of the scanner, while scanning one line after another.

Fourier transform may be used whenever the frequency (of the features), either in the reciprocal time or wave number, is of importance [Whi 94]. Fast Fourier transform (FFT) is an algorithm that has been developed to compute the direct Fourier transforms more efficiently. FFT is used in digital filtering specially for images with periodic structures, as their symmetry properties and the spacing of features can become clearly visible using this method. An example of that is shown in fig. 4.13.

The FFT was used in this study to examine the periodicity of the surface structures in the AFM images. The power spectrum is derived by performing a fast Fourier transform on each line in the direction chosen in the transform selection and then normalizing the results for all the lines. An inverse FFT can be performed to eliminate unwanted (noise) frequencies in the power spectrum to give a filtered image as illustrated in the figure 4.13(d).

The centre of the high intensity spot in the power spectrum associated with the FFT, which approximately gives the average wavelength, was also recorded.

In figure 4.13(b) and 4.13(d) the origin of the reciprocal space is in the centre of the spectrum. The two high intensity spots located on the equator line show that there is a periodicity in the original image. The two circles near the centre of the power spectrum fig. 4.13(b) were used to choose the frequencies of interest in other words the dominant frequencies. Applying an inverse Fourier transform the filtered image only contains features corresponding to the frequencies chosen and eliminates the other features.

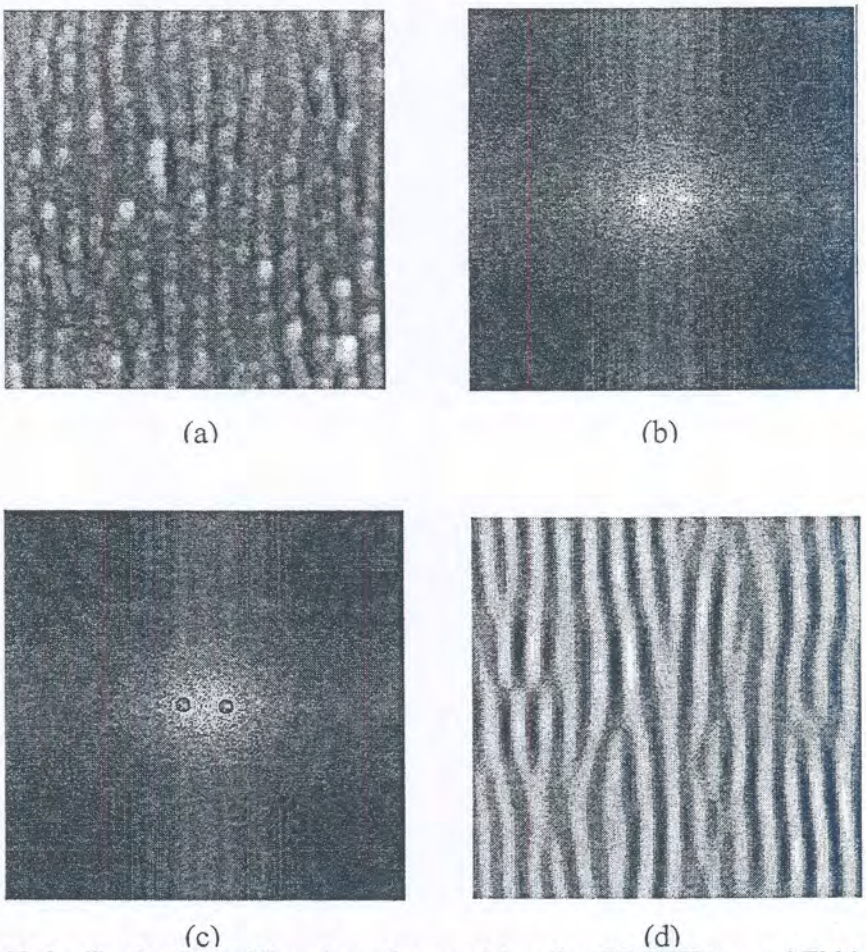

Figure 4.13 An illustration of the steps for applying the 2D FFT to an AFM image (Φ =2 x 10^{19} Ar^+ /cm^2) (a) the original image (b) the power spectrum (c) chosen frequencies (d) filtered image.

Fig. 4.14 shows the way used for measuring the wavelength from the AFM images. The distance from point 1 to point 2 was measured (1958 μm) and the number of peaks between the two points (7 peaks) was counted. The wavelength was determined by dividing the distance by the number of peaks (0.28 μm). This method was used to reduce the error that might occur when deciding where the feature starts and where it ends.

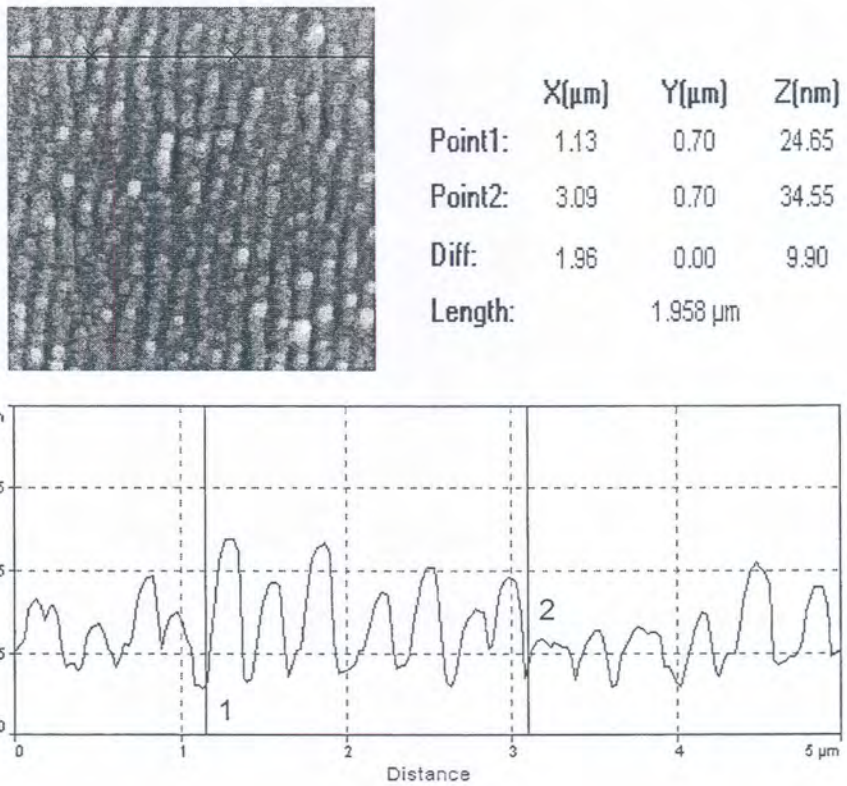

Fig. 4.14 Measuring the wavelength from a line profile in an AFM image for argon bombarded InP ($\Phi = 2 \times 10^{19}$ ions/cm^2).

4.3.5 Artifacts in SPM images

The roughness analysis can be strongly biased by imaging artifacts, which is the term usually used to describe defects in the acquired data (image). Many tip artifacts in AFM images arise from spatial convolution of the shape of the tip and the shape of surface features imaged [Fro 01]. If the radii of curvature of the surface asperities are comparable to the radius of the tip apex, the shape of the tip will significantly determine the measured topography.

A number of studies [Sea 99], [Sea 00], [Fro 01] were done to evaluate and define the shape of AFM tips using the cones formed during sputtering. The shape of the tip is determined using software that averages the images of several individual cones allowing the tip to be monitored, wear effects to be diagnosed and worn tips to be replaced. The above-mentioned work shows that the finite size of the tip filters the high frequency components of the topographic features and in some cases cause inaccuracy in the measurements [Sed 01].

Another cause of SPM image artifacts is the acquisition process that affects the roughness calculations. For example, the piezoelectric scanner movement, which is not parellel to the scanning plane can result in artefacts in the roughness calculations (see fig. 4.7) . That is the reason why SPM usually have planar artifacts that is not representative of the surface. Removing of artifacts will also result in misrepresentation. An additional source of artifacts could be minor temperature fluctuations, optical interference in the detection system, and non-linearity in the x-y motion of the piezoelectric scanner, random tip jumps and the tip geometry change as a result of picking a dust particle or ad-atoms from the surface under investigation.

In some images when observing different topographical features, to investigate whether the structures observed are real or resulting from artifacts, the scanning was done in different scanning directions and images were compared.

The results from the 7 x 7μm^2 scan ranges were excluded. When maximum scanner range is used, the mechanical movement of the scanner significantly affects the movement of the tip near the edges of the areas under investigation (jump of the tip).

4.4 SEM and AFM: Complementary techniques for surface investigations

There is a wide range of analytical techniques that could be used for material characterization depending on the information needed. Two commonly used techniques for high-resolution surface topography investigations are Scanning Electron Microscopy (SEM) and Atomic Force Microscopy (AFM). Each of these techniques has a different mechanism for image formation resulting in different types of information about the surface structure under study. One principle difference between the two techniques is how they process vertical changes in the topography.

For SEM images, the electron beam interacts with the near surface region of the specimen to a depth of approximately 5-10 nm and generates signals that are used to form an image. Observing the different features depends on the intensity (number) of the secondary electrons emitted from a certain part of the surface and observing a three dimensional object depends on depth of field. A high depth of field is obtained

when the different heights in the image of a rough surface are all in focus at the same time.

For the FE-SEM images a large area view of the variations of surface structure can be acquired in a short time. The reason for that is when you focus the electron beam and you move to another part of the sample the new part will still be more or less in focus. The time needed for the acquisition of the SEM image is very short in comparison with the AFM. In general, AFM only scans over a relatively small area of the surface. Tilting the sample with respect to the electron beam in SEM gives more information about the shape of the features but quantification measurements are not easy. One has to consider the tilting angle, because the magnification perpendicular to the tilting axis becomes unreal (it is not possible to use the magnification bar to directly measure length). In the SEM image changes in the slope can result in an increase or decrease in secondary electrons emission from the sample surface, producing a high intensity in the image making it sometimes difficult to determine whether the feature is slopping up or down. Another problem with the SEM is that the electron beam penetrates few layers (the accelerating voltage used in this study was 5 kV), so the information in the SEM images is not only from the surface.

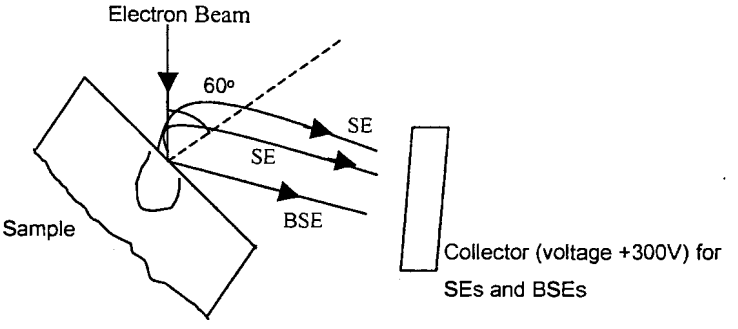

Fig.4.15 Tilting the samples 60° in the SEM.

For AFM the mechanical movement of the tip over the surface gives a more accurate observation of the surface heights. However, the artifacts discussed in 4.3.5 sometimes limit this accuracy. The three-dimensional nature of the AFM images makes it possible to calculate the surface roughness parameters and it can determine whether the features are bumps or pits [Rus 01].

Both the SEM and the AFM have image artifacts, so by using the two techniques together, one technique will often compensate for the imaging artifacts of the other technique.

References: Chapter 4

[Bar 89] T. T. Bardin, J. G. Pronko, A. J. Mardinly and C. R. Wie, *Nucl. Instrum. Meth. Phys. Res.* B 40/41 (1989) 533.

[Bin 86] G. Binning, C. F. Quate and Ch. Gerber, *Phys. Rev. Lett.* 56 (1986) 930.

[Dem 95] C. M. Demanet, J. B. Malherbe, N. G. van der Berg and K. Vijaya Sankar, *Surf. Interface Anal.* 23 (1995) 433.

[Dem 96a] C. M. Demanet, K. Vijaya Sankar, J. B. Malherbe, N. G. van der Berg and R. Q. Odendaal, *Surf. Interf. Anal.* 24 (1996) 497.

[Fan 96] S. J. Fang, W. Chen, T. Yamamaka and C.R. Helms, *Appl. Phys. Lett.* 68 (1996) 2837.

[Fan 97] S. J. Fang, S. Haplepete, W. Chen, and C. R. Helms, *J. Appl. Phys.* 82 (1997) 5891.

[Fro 01] F. Frost, D. Hirsch and A. Schindler, *Appl. Surf. Sci.* 179 (2001) 8.

[Gol 92] J. I. Goldstein, D. E. Newbury, P. Echlin, D.C. Joy, C. Fiori, J. and E. Lifshin, in *Scanning Electron Microscopy & X- Ray Microanalysis*, 1981 Plenum Press, New York (1992) Chapter 2.

[Joy 84] D. C. Joy, *J. Microscopy* 136 (1984) 241

[Kie 97] J. D. Kiely and D. A. Bonnell, *J. Vac. Sci. Technol.* B 15(4) (1997) 1483.

[Liu 03] D. P. Liu, G. Benstetter, Y. H. Liu, J. L. Zhang, C. S. Ren and T. C. Ma, *Surf. Coating Technol.* 174-175 (2003) 310.

[Mal 81] J. B. Malherbe, J. M. Sanz and S. Hofmann, *Surf. Interface Anal.* 3 (1981) 235.

[Mal 91] J. B. Malherbe, H. Lanker and W. H. Gries, *Surf. Interface Anal.* 17 (1991) 719.

[Mal 94] J. B. Malherbe, *CRC Crit. Rev. Solid State Mater. Sci.* 19 (1994) 129.

[Pan 98] J. S. Pan, S. T. Tay, C. H. A. Huan and A. T. S. Wee, *Surf. Interface Anal.* 26 (1998).

[Rug 90] D. Rugar and P. Hansma, *Phys. Today* (1990) 23.

[Rus 01] P. Russel, D. Batchelor and J. Thornton, *Asia/Pacific Microscopy and Anal.* (2001) 13.

[Sea 99] M. P. Seah, S. J. Spencer, P. J. Cumpson and J. E. Johnstone, *Appl. Surf. Sci.* 144-145 (1999) 151.

[Sea 00] M. P. Seah, S. J. Spencer, P. J. Cumpson and J. E. Johnstone, *Surf. Interface Anal.* 29 (2000) 782.

[Sed 01] D. L. Sedin and K. L. Rowlen, *Appl. Surf. Sci.* 182 (2001) 40.

[Spa 94] L. Spanos and E. Irene, *J. Vac. Sci. Technol.* A 12 (1994) 2646.

[Tan 90] M. Tanemura, S. Fujimoto and F. Okuyama, *Surf. Interface Anal.* 15 (1990) 537.

[Top 00] TopoMetrix user manual, Version 3.05.

[Weh 85] G. K. Wehner, *J. Vac. Sci. Technol.* A 3, (1985) 1821.

[Whi 94] D.J. Whitehouse, in *Handbook of Surface Metrology*, published by Institute of Physics Publishing, Bristol and Philadelphia (1994).

[Zym 00] D. Zymierska, J. Aueytner, T. Kobiela and R. Dus, *Phys. Stat. Sol.* 180 (2000) 479.

Chapter 5

Experimental Investigation Of Nitrogen-Bombarded InP Topography Dependence on the Areic Dose

5.1 Introduction

In this chapter the evolution of the InP surface topography after ion bombardment was investigated. 1x1μm^2 FE-SEM and AFM images are presented. Two (2D) and three-dimensional (3D) images for the AFM images were used. A quantification of the AFM images was done in terms of the average values of maximum height R_p above mean line, the maximum peak to valley height R_t, the root mean square roughness R_{rms}, fractal dimension (FD) and the roughness factor. Using the number of cones calculated from the lake filling method the density of cones is also reported in this chapter. The average area of the cones from arbitrary line profiles from the surface was also measured. Fast Fourier transforms (FFT) were used to examine the beginning and the development of the regular features with increasing the areic dose.

FE-SEM images are only discussed for doses equal to and higher than 5 x 10^{14} N_2^+/cm^2. The reason for that is for the lower doses (see fig. 5.4 (c)) the FE-SEM did not show anything but a flat surface.

Surface roughness parameters were studied and their behaviour with increasing the areic doses was investigated (see graphs in figures.4.10 – 4.16).

5.2 Results 1; AFM and SEM images

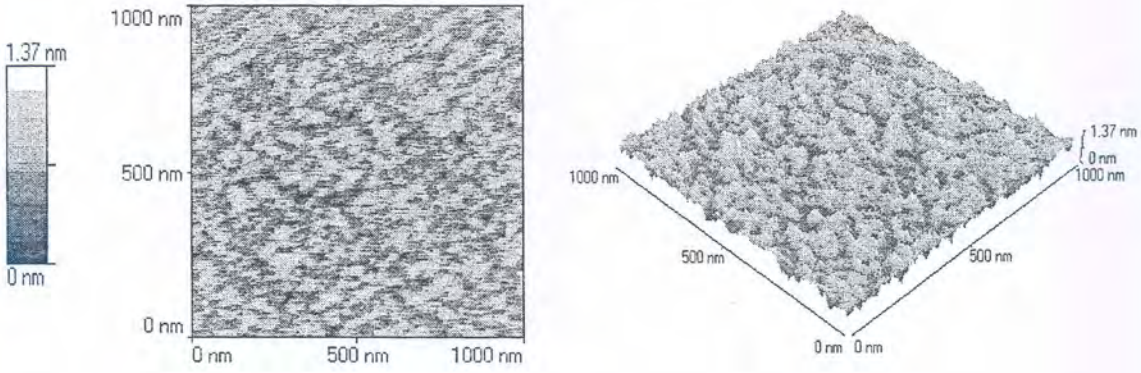

Fig. 5.1 2D and 3D AFM images of an unbombarded, as received from factory InP surface.

Fig. 5.1 shows a two-dimensional AFM image of an InP sample (as received from factory) before ion bombardment. The line measurements showed that the value for R_t = 0.77 nm and the R_p = 0.36nm.The roughness factor is ~1.01, the fractal dimension is ~2.89 and the R_{rms} is 0.25 nm. The measured roughness values for the un-bombarded samples were used as reference values in figures 5.10 to 5.16.

The evolution of surface topography is shown in figures 5.2 to 5.9 with increasing the areic dose. Two and three-dimensional AFM images of 1x1□m² areas and the corresponding FE-SEM (not necessary the same area on the surface) images of 1x1□m² scan area. The FE-SEM images presented were obtained with the electron beam perpendicular to the sample surface and when electron beam was tilted 60° (5 x 10^{15} N_2^+/cm² ≤ Φ ≤ 1 x 10^{17} N_2^+/cm²) or 30° (Φ = 5 x 10^{15} N_2^+/cm²) to the samples normal.

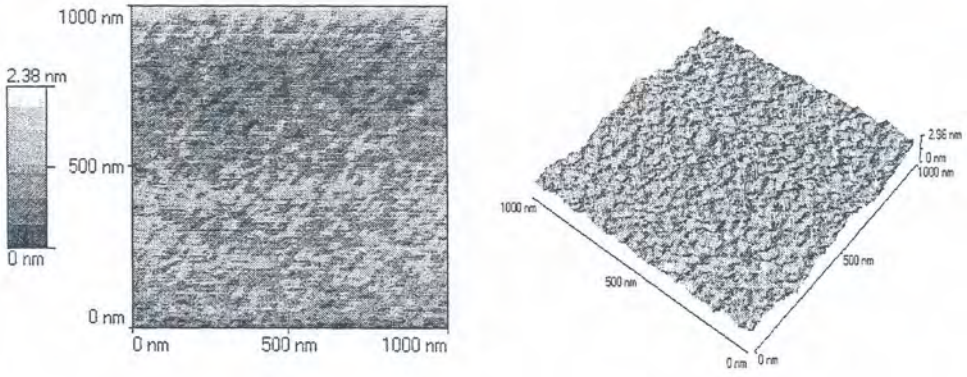

(a) *(b)*

Fig. 5.2 (a) 2D and the corresponding (b) 3D AFM image for $\Phi = 1 \times 10^{14} N_2^+ / cm^2$.

For the sample bombarded to areic dose of $\Phi = 1x10^{14} N_2^+ / cm^2$, the AFM images of the bombarded surface did not show any cone formation. The surface heights were not significantly different from those of the unbombarded samples (see height scale bars fig. 5.1 and fig. 5.2). Line and area measurement values obtained for these samples were different and did not agree from one area of scan to another. A probable reason could be that the value calculated was a result of measuring the substrate surface curvature and not the fine structure of the flat topography.

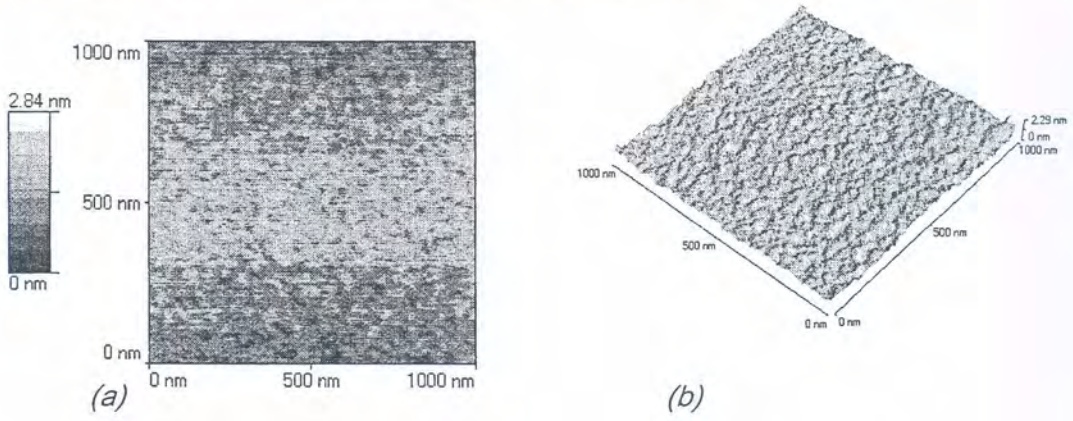

Fig. 5.3 (a) 2D and the corresponding (b) 3D AFM image for $\Phi = 5 \times 10^{14} N_2^+ / cm^2$.

From fig. 5.3 it is clear that up to this dose no significant structures or height differences was observed. The height scale is approximately the same as the one for the un-bombarded sample (see height scales from the AFM images).

Figure 5.4 shows that bombarding the samples to an areic dose of Φ = 1X10^{15} N_2^+/cm^2 do not result in any height or topographical change compared with the unbombarded surfaces. The FE-SEM image 5.4(c) showed a very flat surface. This observation shows that the AFM is more sensitive to fine topographical structures with very small heights. The reason for that is given in detail in the discussion chapter.

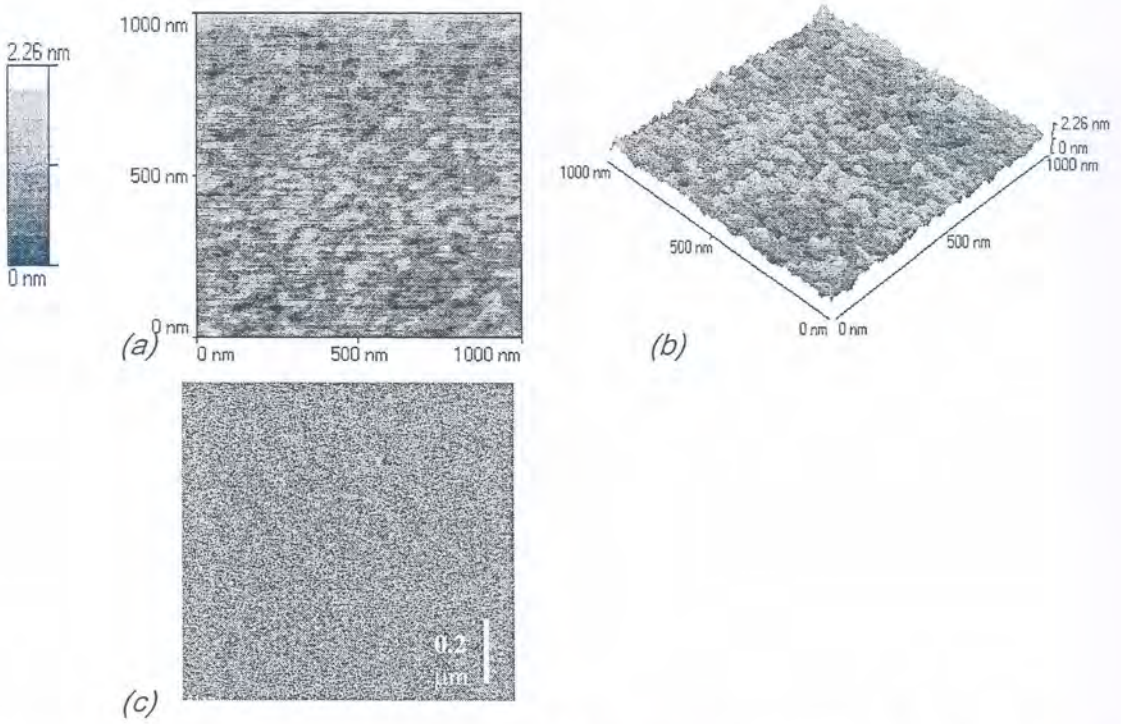

Fig. 5.4 (a) 2D and the corresponding (b) 3D AFM image and (c) the FE-SEM image for $\Phi = 1 \times 10^{15} N_2^+ / cm^2$

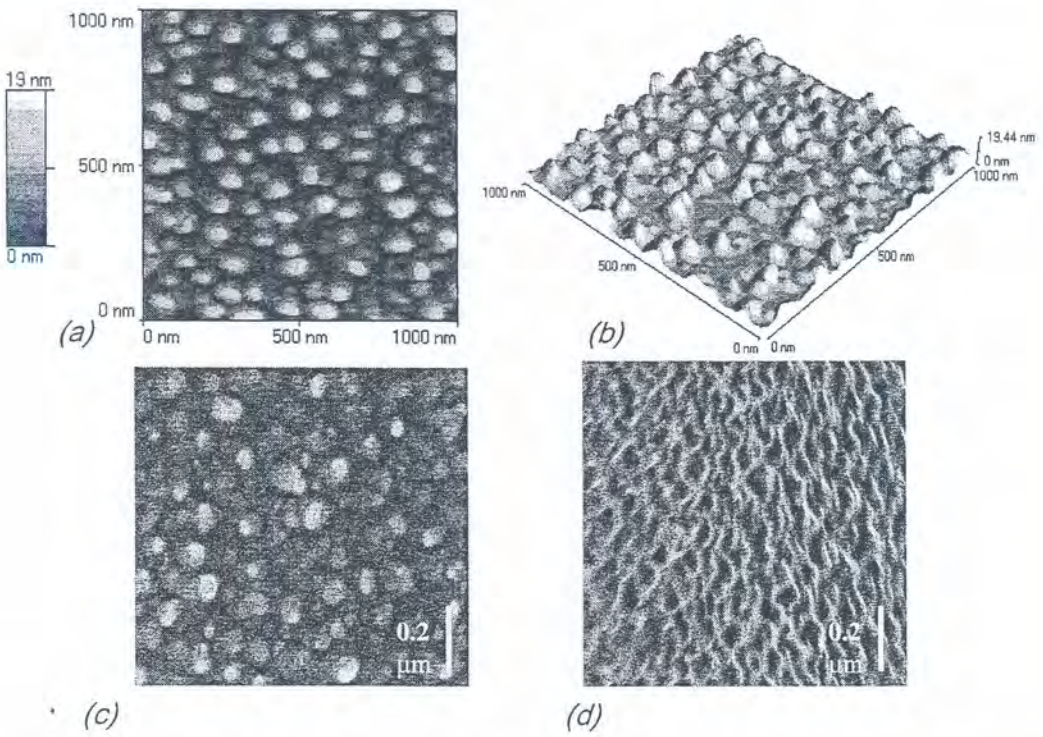

Fig. 5.5 (a) 2D and the corresponding (b) 3D AFM image and (c) the FE-SEM (d) FE-SEM image when electron beam made an angle of 60° to the sample normal, for $\Phi = 5 \times 10^{15} N_2^+ / cm^2$.

From figures 5.5(a), (b), (c) and (d) bombarding the sample with nitrogen to an areic dose of $\Phi = 5\times10^{15}$ N_2^+/cm^2. resulted in a rough surface with cones of two different heights (14 and 11 nm) and diameters (100 and 80 nm). One could assume that the cones could start at an earlier stage of sputtering ($1x10^{15}$ $N_2^+/cm^2 \leq \Phi \leq$ $5x10^{15}$ N_2^+/cm^2). The other observation is that the surface is not completely covered with cones but there exist open spaces between the cones (see fig. 5.5(b), 5(c)). FE-SEM shows the peak of the cones to be brighter than the base. The physical meaning of that is that the cones have steep walls. There is a correlation between the AFM and FE-SEM images. Comparing figures 5.5(a) and 5.5(c), the two types of cones are visible in the two images and they seem to approximately have the same size. The FE-SEM and AFM images are not necessary from the same area of the sample but due to the homogenous bombarded area they showed the same kind of topographical features.

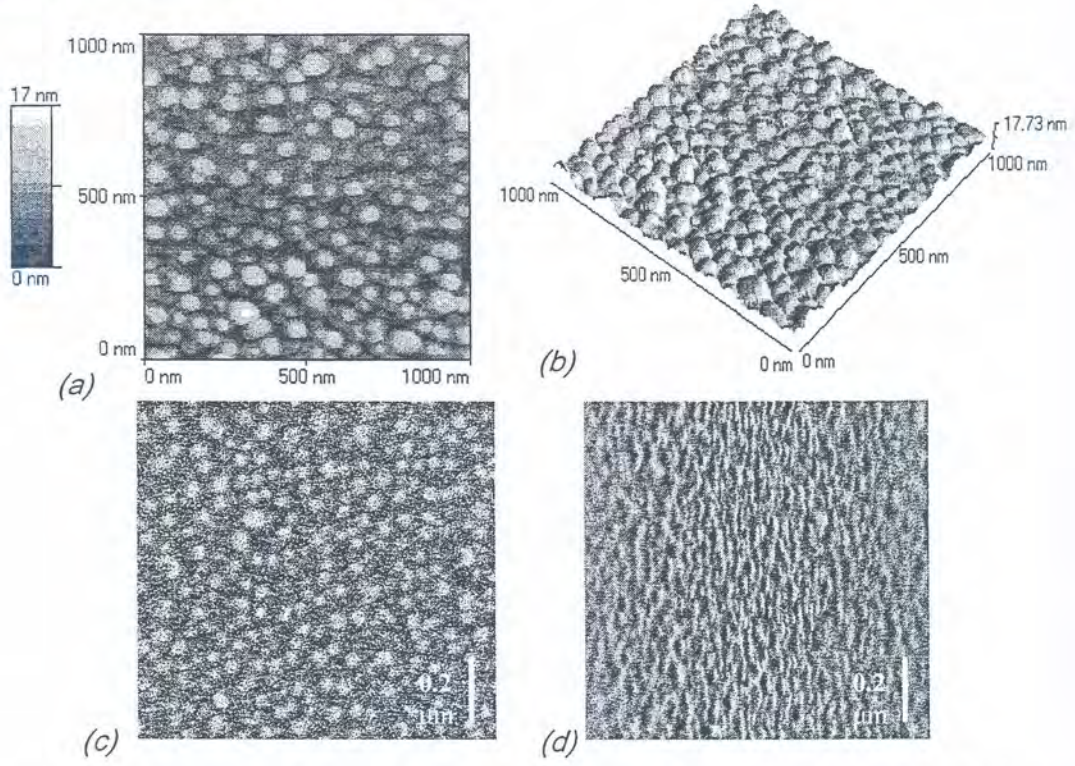

Fig. 5.6 (a) 2D and the corresponding (b) 3D AFM image and (c) the FE-SEM (d) FE-SEM image when electron beam made an angle of 60° to the sample normal, for the areic dose $\Phi = 1\times10^{16} N_2^+ / cm^2$.

Bombarding the sample with $\Phi = 1\times10^{16} N_2^+ / cm^2$ it was observed that the height scale does not differ from the previous areic dose.

Increasing the areic dose to $\Phi = 5\times10^{16} N_2^+ / cm^2$ caused the cones to grow in size and more significantly in heights (see fig. 5.7(a) to 5.7(d)). Again there appear to be two types of cones small and larger ones.

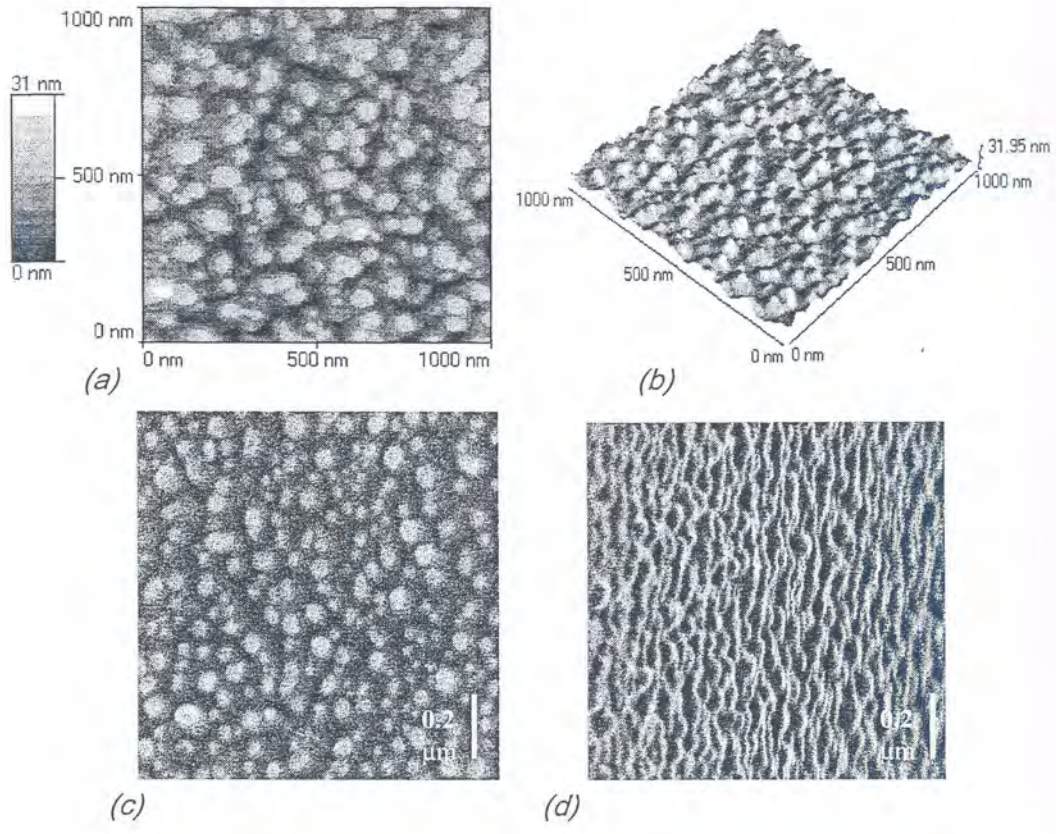

Fig. 5.7 (a) 2D and the corresponding (b) 3D AFM image and (c) the FE-SEM (d) FE-SEM image when electron beam made an angle of 60° to the sample normal, for $\Phi = 5\ x10^{16}\ N_2^+ /cm^2$.

Increasing the areic dose to $\Phi = 1\times10^{17}$ N_2^+/cm^2 does not seem to change the induced topography more than that of $\Phi = 5\times10^{16}$ N_2^+/cm^2. The cones shape and size and density stayed nearly the same.

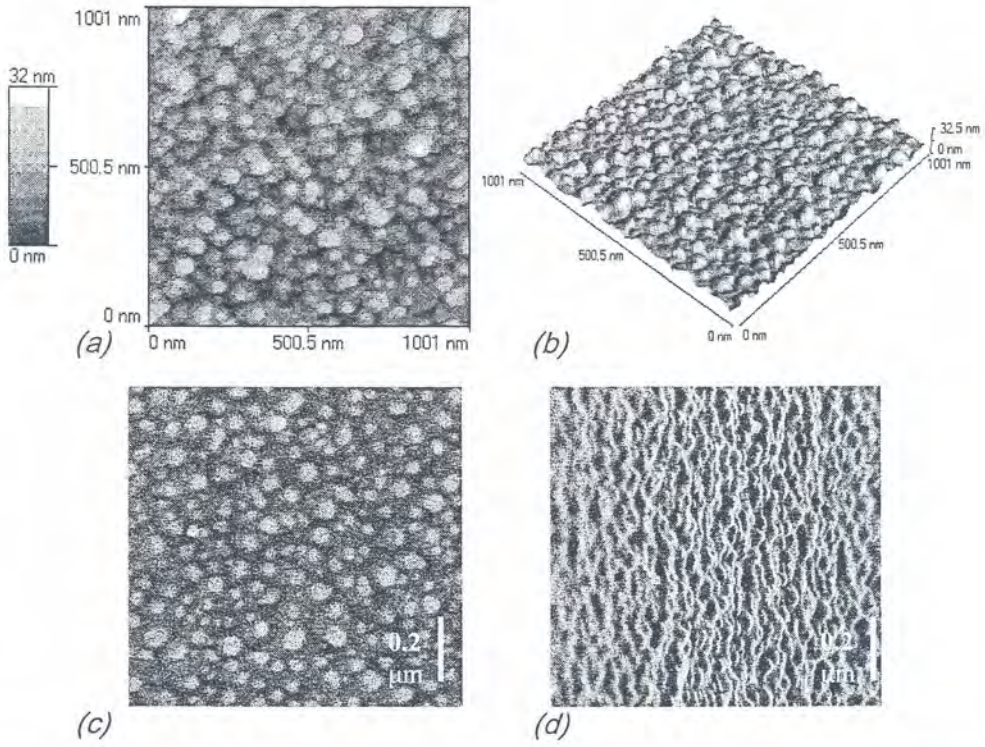

Fig. 5.8 (a) 2D and the corresponding (b) 3D AFM image and (c) the FE-SEM (d) FE-SEM image when electron beam made an angle of 60° to the sample normal, for $\Phi = 1 \times 10^{17} N_2^+ /cm^2$.

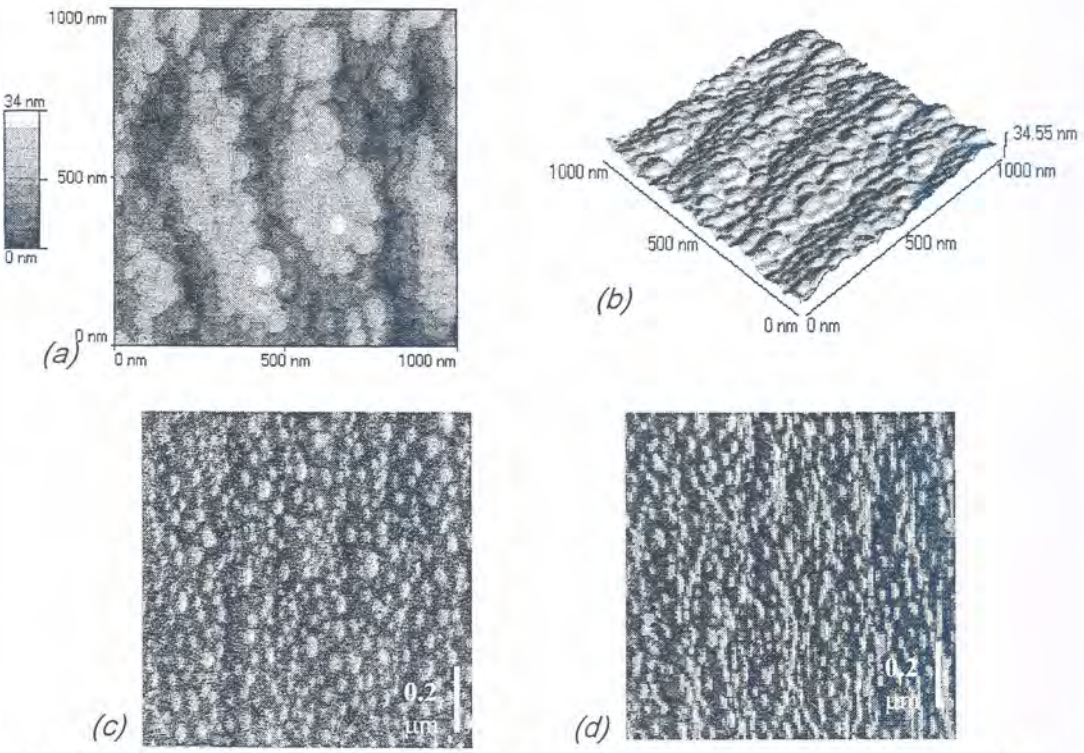

Fig. 5.9 (a) 2D and the corresponding (b) 3D AFM image and (c) the FE-SEM (d) FE-SEM image when electron beam made an angle of 30° to the sample normal, for $\Phi = 5 \times 10^{17} N_2^+ /cm^2$.

Bombarding the sample with nitrogen to an areic dose of $\Phi = 5 \times 10^{17} N_2^+/cm^2$ clear ripples was visible in the AFM images and the tilted FE-SEM image. The ripples consist of cones with (approximately) the same areas and shapes as the ones for the lower areic doses (see fig. 5.9). From the shapes of the cones (AFM images) it seems as if the cones merge across the surface to form the ripples.

It was observed from fig. 5.9 that, ripples with a wavelength of ~0.23 μm and amplitude of ~ 0.15-0.2 μm appear on the sputtered surfaces for Φ = 5x10^{17}N_2^+/cm^2. The direction of the ripples is parallel to the surface component of the ion beam direction in agreement with the Bradley-Harper theory [Bra 88]. The average wavelength of the ripples was determined by dividing the total distance by the number of ripples (from three different line profiles along each image).

General comment from figures 5.2 to 5.9: -

For some of the 3D AFM images shadows were added to the images create better contrast. Bombarding InP (100) with 5 keV N_2^+ at 41^o there was an increase in the surface roughness with increasing the areic dose in the range of Φ = 1x10^{15} N_2^+/cm^2 $\leq \Phi$. $\leq$ 5 x 10^{17} N_2^+/cm^2 For low doses bombardment (1x10^{14} - 1x10^{15} N_2^+/cm^2) it was observed that the surface roughness was approximately the same as that of the virgin InP and some times it is even lower (see figures (5.2, 5.3, 5.4, 5.10 - 5.16)). This could be explained as a result of the amporhization that (as discussed in chapter 5.6) is assumed to take place for low areic doses ion bombardment (as discussed in chapter 6).

For doses higher than 1x10^{15} N_2^+/cm^2, the cones started as small protuberances (~4-6 nm in height and area of~ 3100 nm^2 see fig. 5.2, 5.3, 5.4 and grow in number (fig. 5.5, 5.6, 5.7, 5.8) and height with increasing the areic dose to 1x10^{17} N_2^+/cm^2. It was observed that for the doses of 5x10^{16} – 1x10^{17} N_2^+/cm^2 there was an equilibrium (saturation) in the cones state (for e.g. density and height) see figures 5.7 & 5.8. For the areic dose Φ = 5 x 10^{17} N_2^+/cm^2 the increase in the size and density of the cones cause them to collapse and merge towards one another. The merging of cones forms an overall smoother surface with visible ripple structures (fig. 5.9). This statement is confirmed by the results from fig. 5.12. It is shown that the area of the cones is getting smaller as a result of its merging. The density from fig. 5.11 decreased and the roughness factor fig. 8 also decreased as a result of the smoothing of the surface.

It was observed that for low doses (1 x 10^{14} – 5 x 10^{15} N_2^+/cm^2 see fig. 5.4(c)) the FE-SEM images showed a flat surface and it looked the same as the surface of the un-bombarded InP wafers, while the AFM images showed that the surfaces are not completely flat. A logical explanation is that the electron beam in the FE-SEM penetrates the surface and give information (secondary electrons) from the surface and few layers below the surface, so its not very sensitive to small changes in surface heights. From this we can conclude that AFM is a more sensitive to investigate topographical changes than the FE-SEM.

5. 3 Results 2; Roughness parameters as a function of areic dose

Using the TopoMetrix v3.06.06 image analysis package the maximum peak to valley heights in the line profiles (R_p), the maximum heights of the profiles above mean lines (R_t), cones density(d), average cone area, the root mean square roughness R_{rms}, fractal dimension (FD) and the roughness factors were calculated for each areic dose. The results are summarized from fig. 5.10 to fig. 5.16, where the roughness parameters were plotted as a function of areic doses in each case. For all the graphs every data point is an average value taken from at least five AFM images and the error bar represents the standard deviation. For line measurements three arbitrary line profiles were used on each AFM image. The values for the virgin InP(■) is plotted as the values for 1x10^{13} (ions/cm^2).

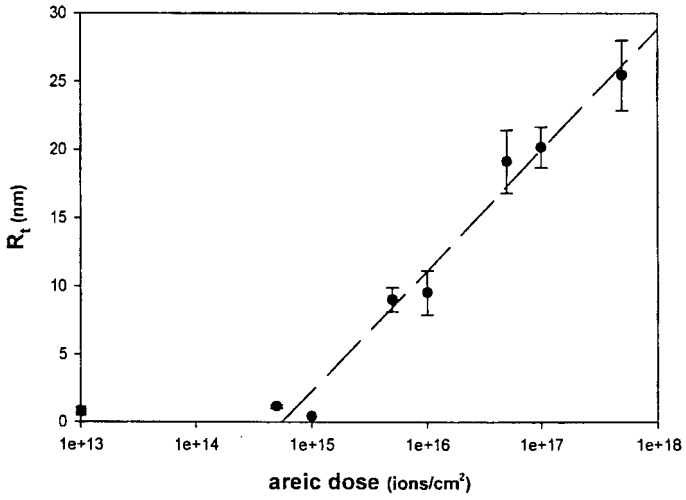

(a)

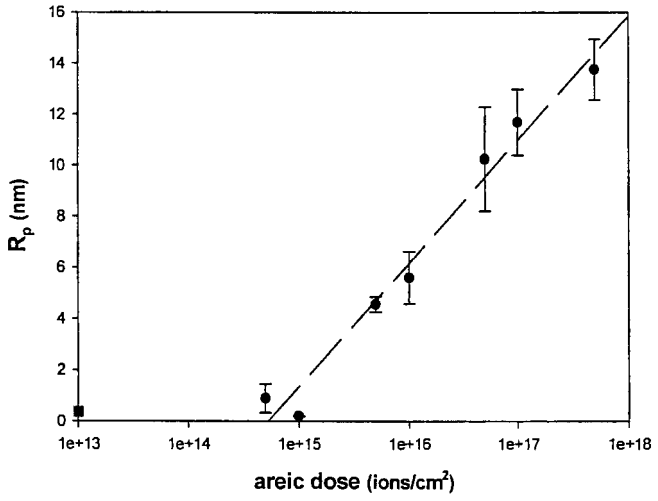

(b)

Fig.5.10 (a) R_t and (b) R_p as a function of the ion areic dose Φ. A linear regression line was fitted for the data range. For R_t the slope is 8.85 and for R_p the slope is 4.83

From fig. 5.10(a) and (b) it is shown that the parameters R_t and R_p increased with increasing the areic dose and they have a linear dependence on the logarithm of the areic dose.

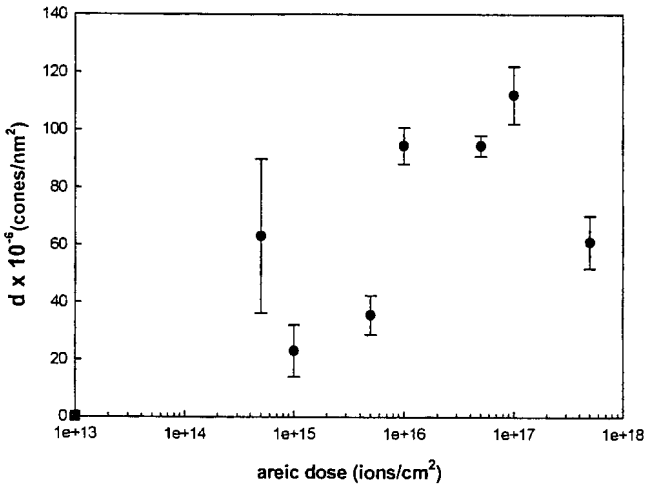

*Fig. 5.11 The surface density of cones (*d*) as a function of the ion areic dose* Φ *.*

The density of the cones over 1x1μm^2 areas of the sample generally increased with increasing the areic dose (see fig. 5.11). The inaccuracy of the lake filling method used to calculate the number of cones is the reason for the large error bars for Φ = 5 x10^{14} N_2^+/cm^2. This inaccuracy appears mostly for the relatively flat surfaces and for samples with original surface curvatures. In figures 5.11 and 5.12 the values of the unsputtered samples is zero because the unsputtered sample got no cones or other features.

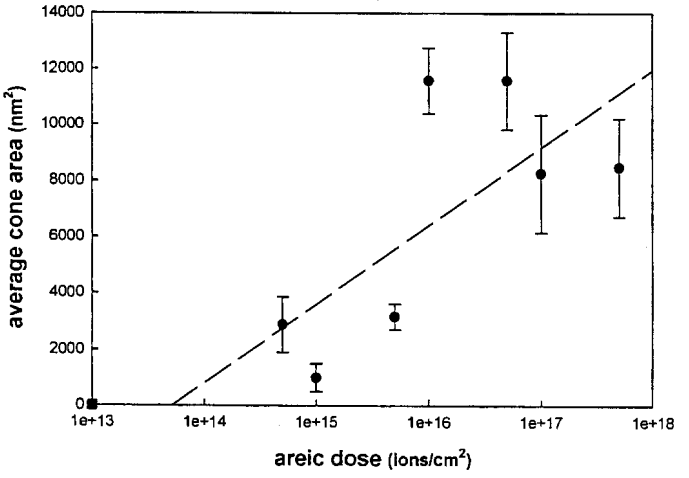

Fig. 5.12 The average area of the cones as a function of the ion areic dose Φ *. A linear regression line was fitted for the data range. The slope is 2787.6.*

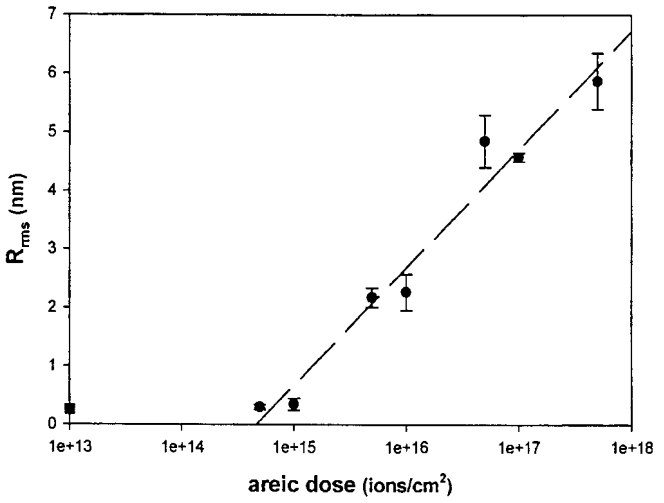

Fig. 5.13 The surface root mean square roughness as a function of the ion areic dose Φ. A linear regression line was fitted for the data range. The slope is 2.01

In fig. 5.13 the R_{rms} value was measured over an area of 1×1 μm^2. A linear regression line was fitted. The error bars correspond to the statistical variation for the five values from the average R_{rms}.

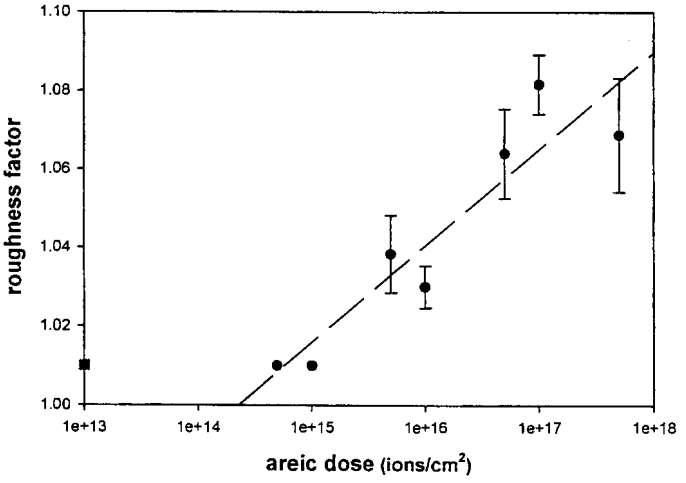

Fig. 5.14 The surface roughness factor as a function of the ion areic dose Φ. A linear regression line was fitted for the data range. The slope is 0.024.

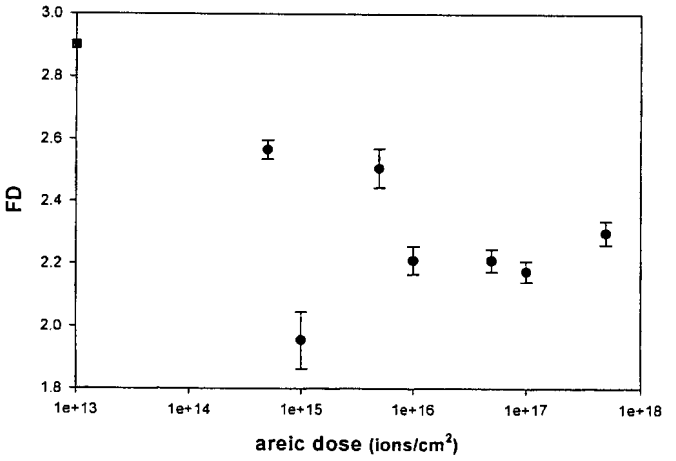

Fig. 5.15 The surface fractal dimensions (FD) as a function of the ion areic dose Φ.

In all the above graphs (fig. 5.10- fig. 5.15) the roughness values were measured over an area of 1×1 μm^2. The error bars correspond to the statistical variation for the five values from the average values.

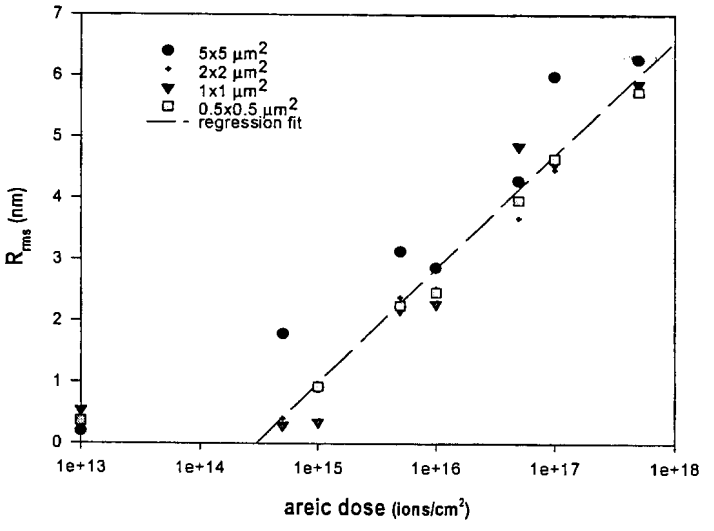

Fig.5.16 Surface roughness(nm) measured for different scan ranges shown as a function of areic dose Φ (ions/cm²). A linear regression line was fitted for the data range. The slope is 1.81.

The R_{rms} calculated from different scan ranges is plotted as a function of areic dose in fig. 5.16. the important observation is that, it was possible to fit all the data points into one straight line.

5.4 Results 3; FFT and ripples wavelength measurements

In fig. 5.17 AFM 2D gray scale images of InP before sputtering, and after sputtering with nitrogen, from scan area 2 x 2μm^2 and the corresponding FFT spectra of the AFM images are presented. In the sputtered samples' images an arrow indicates the direction of the ion beam.

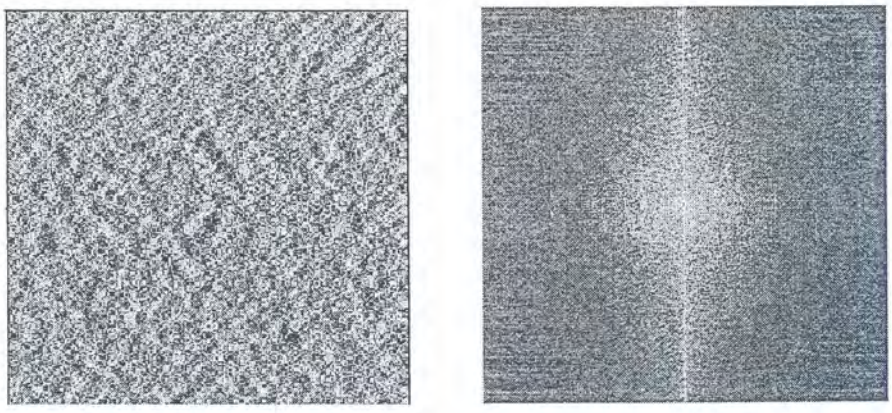

(a) un-sputtered

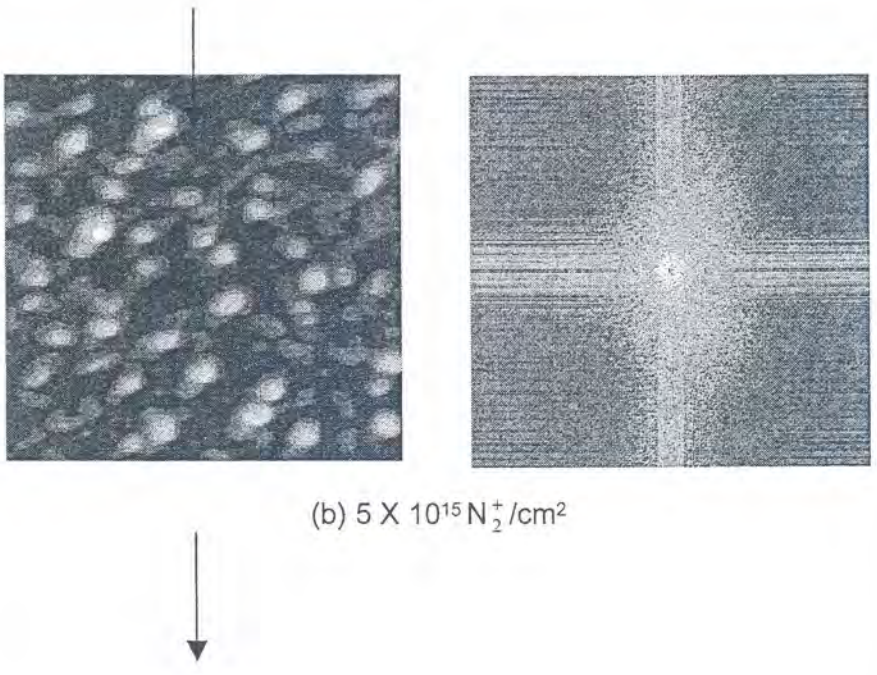

(b) 5 X $10^{15} N_2^+/cm^2$

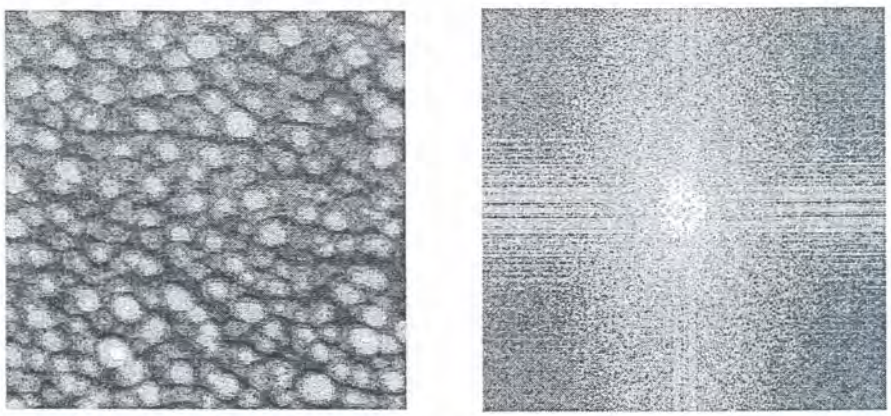

(c) 1 X 10^{16} N_2^+/cm^2

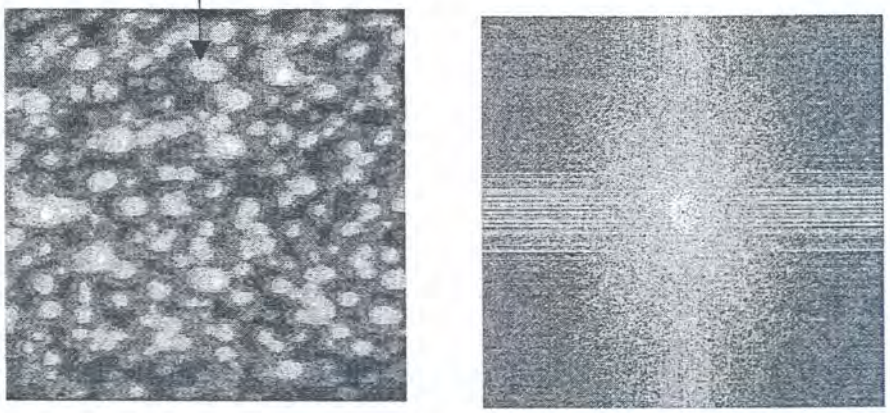

(d) 5 X 10^{16} N_2^+/cm^2

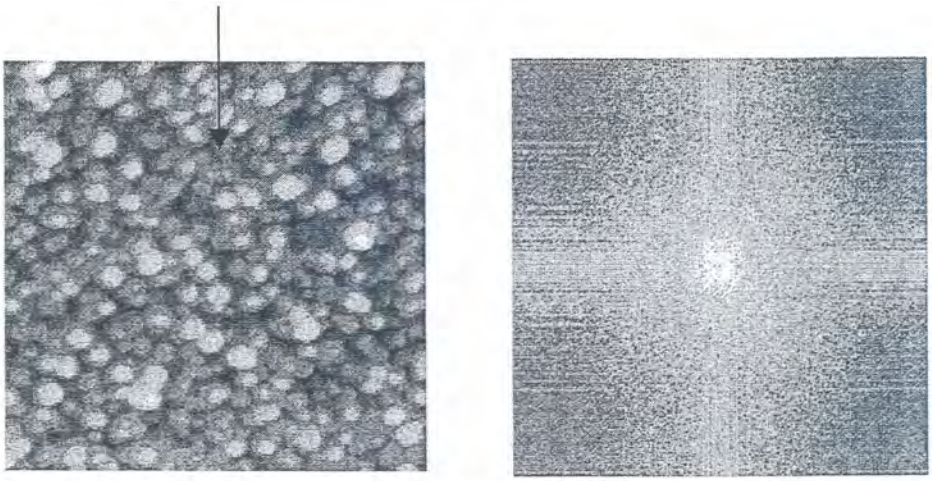

(e) 1 X 10^{17} N_2^+/cm^2

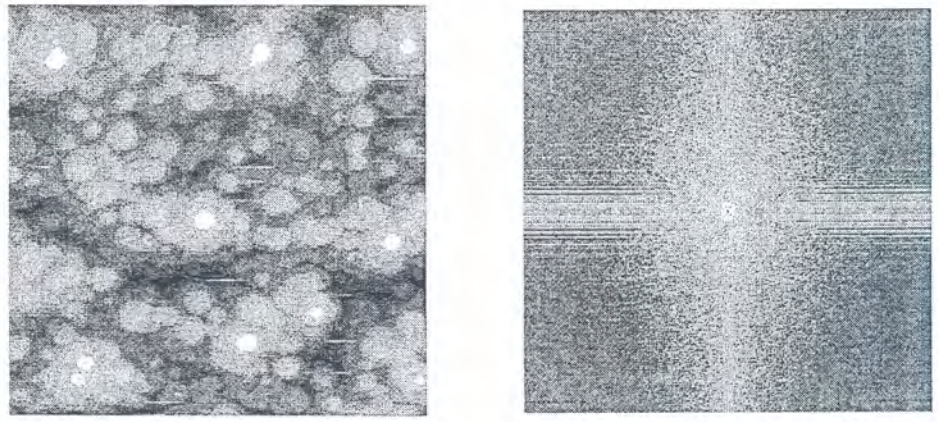

(f) 5 X 10^{17} N_2^+/cm^2

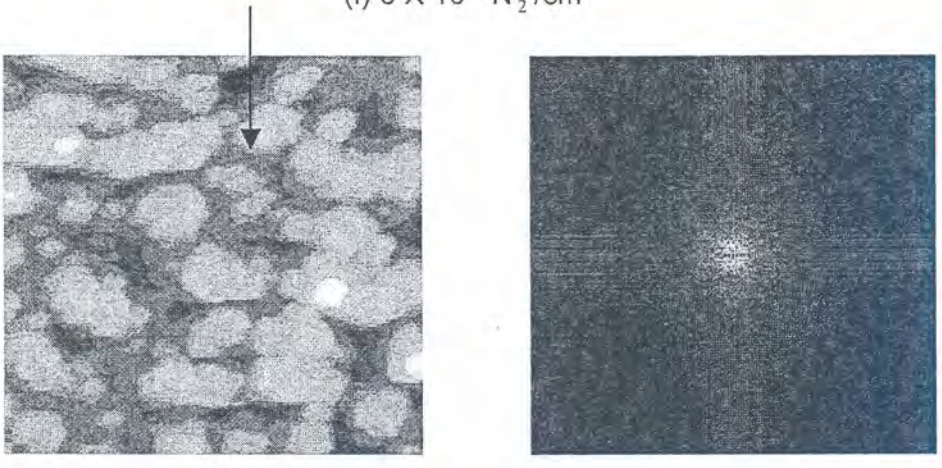

(g) 1 x 10^{18} N_2^+/cm^2

Fig. 5.17 AFM 2D grey scale images and the corresponding FFT spectra of InP (a) before sputtering, and after sputtering of the areic doses (b) 5 x10^{15}, (c) 1 x10^{16} (d) 5 x10^{16}, (e) 1 X10^{17}, (f) 5 x10^{17} (g) 1 x 10^{18} N_2^+ */cm^2, from scan area 2x2 μm^2 .*

Table 5.1: *The wavelength values measured directly from AFM Images and the values measured from the power spectrum for the 2D FFT.*

areic dose (N_2^+/cm²)	1 X 10^{16}	5 x 10^{16}	1 x 10^{17}	5 X 10^{17}	1 X 10^{18}
Wavelength measured directly from AFM images (nm)	-	-	-	269.9810	309.5833
Wavelength measured Centre of spot (nm)	142.0000	125.2500	201.7778	291.5333	312.7778

Table 5.1 shows the values measured for the wavelengths. For the higher doses a comparison between the values measured directly from original AFM images and the values measured from the power spectrum of the FFT is presented.

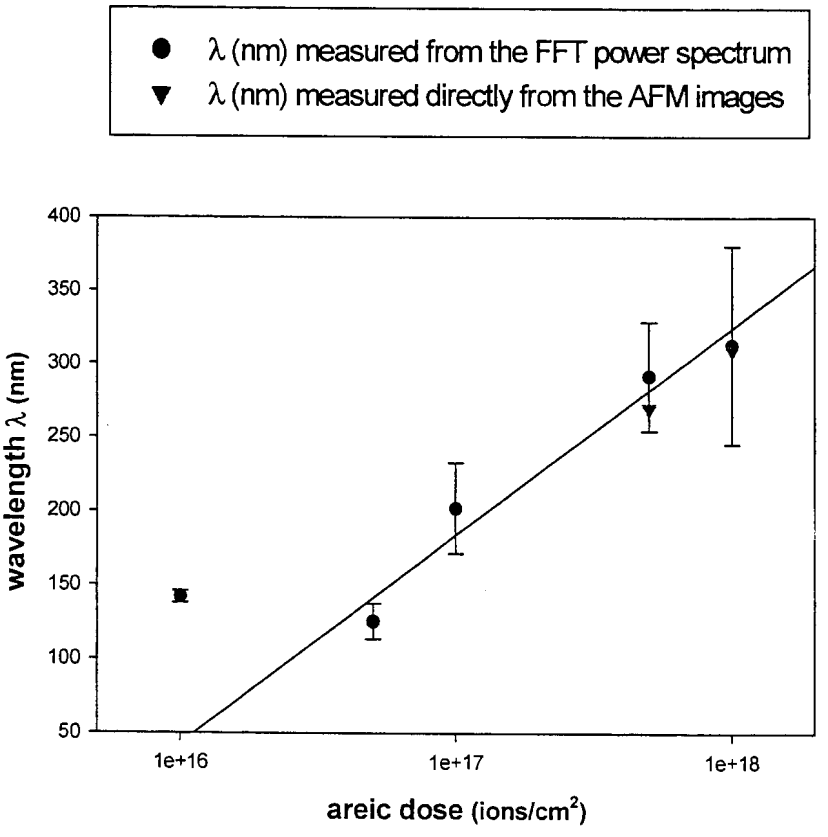

Fig. 5.18 The surface wavelength (λ) as a function of the ion areic dose Φ.

From fig. 5.18 for 5 x 10^{16} $N_2^+/cm^2 \leq \Phi \leq 1$ X 10^{18} N_2^+/cm^2 there was a linear relation between the ripple wavelength measured from the power spectrum associated with the FFT and the logarithm of the areic dose.

References: Chapter 5

[Bra 88] R. M. Bradley and J. M. E. Harper, *J. Vac. Sci. Technol.* A 6 (1988) 2390.

Chapter 6

Discussion

6.1 Introduction

In this study FE-SEM and AFM images were used to investigate surface topography of nitrogen bombarded InP wafers. The FE-SEM was used to give a wide view of the sample under investigation in relatively short times (compared with the AFM). The main information that was confirmed by looking at the FE-FEM images is that the sputtered areas for all the samples consist of homogenous structures (same kind of structures in every place of the sputtered areas). Atomic force microscopy AFM, which gives quantitative topographical information with better spatial resolution than scanning electron microscopy (FE-SEM), was used to investigate the evolution of the surface topography of InP wafer before and after nitrogen bombardment.

As was discussed in chapter 2, a wide variety of topographical features may develop on surfaces after ion bombardment. Needle-like structures, cones, grooves, ridges, pyramids and sponge surfaces are all examples of the possible features. In this work under the conditions discussed in chapter 4, the only features obtained were the cones and ripples on the bombarded InP surface.

Traditionally in the field of bombardment induced periodic structures (e.g. ripples), the Bradley Harper (B-H) theory is the theory against which the experimental findings are tested [Bra 88]. Two aspects of the B-H are discussed in this chapter. The first is the dependence of the ripple's wavelength on the areic dose. The second is the direction of the ripple wave vector.

The B-H theory suggested that the local surface curvatures of the un-bombarded amorphous sample surface induce instability. This instability leads to the formation of periodically modulated surfaces. Makeev *et. al.* [Mak 02] derived a partial differential equation for the surface heights, which involves up to the fourth order derivative of height and incorporates surface diffusion and the fluctuations arising in the erosion process due to the inhomogeneities in the ion flux. An examination of the beginning of topography development using fast Fourier transform of the AFM images is presented and the results are discussed and compared with the above mentioned statements by Makeev *et. al* . and Bradley *et. al.*

In 6.3 an experimental model for roughness evolution and its dependence on the areic dose will be presented.

6.2 Discussion of the results

This section is a discussion of the results presented in chapter 5.

6.2.1 General points

The first important observation from the FE-SEM and the AFM images is that the topography of the ion-bombarded areas is homogenous. In other words, the bombardment-induced structures have the same shapes and sizes everywhere in the sputtered areas for each areic dose. From figures 5.4 – 5.9 it follows that, there is a correlation between the FE-SEM and the AFM images; however, the AFM images gave more quantitative measurements of the surface heights.

For 1 x 10^{14} N_2^+/cm^2 and 5 x 10^{14} N_2^+/cm^2 the quantitative measurements were not very convincing. There was a large spread in range for the measured values. The reason for that could be the large contribution of the original un-bombarded surface curvatures. The sample surfaces was not completely flat but as a result of the amorphization that takes place the samples appear to be more flat when bombarded to an areic dose of 5x10^{14} N_2^+/cm^2.

As it is shown in figures 5.5, 5.6, 5.7 and 5.8, there are two types of cones: small and larger ones. For the graphs in figures 5.10 to 5.12, the dominant type of cones was used for the measurements. From fig. 5.11, that shows the density of cones on the bombarded surfaces, the large error bar for the areic dose 5x10^{14} N_2^+/cm^2 could be a

result of the inaccuracy of the method used in calculating the number of cones on the surface (see FD chapter 5).

6.2.2 Discussion of roughness parameters

The maximum and mean height variations(R_t and R_p)

The averages of the maximum heights of the arbitrary line profiles above the mean lines variations R_p and the maximum peak to valley heights in the same line profiles height R_t variations increased rapidly (linear fit from 1×10^{15} N_2^+/cm^2) with increasing areic dose.

Cone density and average cone area

From figures 5.2, 5.3 and 5.4, it is clear that for the areic doses 1×10^{14} - 1×10^{15} N_2^+/cm^2 the surface looks flat and the heights of the cone-like features are very small. For the areic dose 5×10^{15} ions/cm² fig. 5.5, well-defined cones with open spaces between them started to appear with heights of ~19 nm. Increasing the dose to 1×10^{16} N_2^+/cm^2 fig. 5.6, the number of cones increased but the heights did not change significantly. The average cone area decreased and there appear to be two kinds of cones smaller ones (area and height) and bigger ones. For the areic dose 5×10^{16} N_2^+/cm^2 fig. 5.7, the density and area of the cones does not change significantly but it grows in height. At the areic dose 1×10^{17} N_2^+/cm^2 fig. 5.8, the surface seems to be more dense with cones. Visible ripples developed when increasing the dose to 5×10^{17} N_2^+/cm^2 and on the ripples there are smaller cones (fig. 5.9).

Generally from fig. 5.11, for areic doses in the range $5x10^{15}$ - $5x10^{17}$ N_2^+/cm^2, the surface density of cones increased up to a dose of $1x10^{17}$ N_2^+/cm^2 and then it went down at a dose of $5x10^{17}$ N_2^+/cm^2.

The average cone area values measured showed the same behavior as the cone density: it increases up to a dose of $5x10^{16}$ N_2^+/cm^2. For $\Phi = 5x10^{17}$ N_2^+/cm^2 and as a result of the surface diffusion the cones areas started to decrease with increasing areic dose (see fig. 5.12).

The root mean square roughness R_{rms} and the roughness factor

The R_{rms} increased linearly with the logarithm of the areic dose (see figures 5.13 and 5.16). Roughness factor showed approximately the same behavior up to an areic dose $\Phi = 1\times10^{17}\ N_2^+/cm^2$. For $\Phi = 5\times10^{17}\ N_2^+/cm^2$ the roughness factor measured values decreased.

Fractal dimensions (*FD*)

If the 3D surface is completely flat the *FD* will be equal to two and as the surface gets rough the value of the *FD* increases. For a completely rough surface *FD* = 3. In our case the *FD* decreased with increasing the areic dose. This means that the surface gets smoother as a result of increasing the ion areic dose. The original surface before bombardment gave the highest value of the fractal dimension (2.89) in comparison with the bombarded samples.

From fig. 5.15 it is shown that the *FD* value for the areic dose $1x10^{15}\ N_2^+/cm^2$ is less than 2. The results obtained using the fractal dimension method did not agree with all the other reported roughness parameters investigated in this study. A probable explanation is that, the TopoMetrix software is incapable of doing an accurate measure for that kind of topography.

6.2.3 Areic dose dependent topography evolution

As was discussed in Chapter 3 there are three different groups of theories and model proposed to explain the mechanisms of cone formation on ion-bombarded surfaces. It is not enough to use sputter-yield based theories or growth theories separately to explain the development of the topographical features in this study.

From fig. (5.13 and 5.16), it is clear that there is a linear dependence of root mean square roughness on the logarithm of areic dose, and not the areic dose, which excludes the seeding sputter erosion model (see Chapter 3) which assumes that the amount of material sputtered away is directly proportional to the areic dose. The same behaviour was observed for inert gas ion bombardment on InP by Demanet *et. al.* [Dem 95].

It is difficult to explain all topographical features consistently. The ion bombardment induced topography is usually a result of a combined number of fundamental roughening and smoothing mechanisms.

One of the major theories developed to explain this phenomenon is the Bradley Harper theory, which relies on a combined model due to the complex process involved during ion-solid interaction. Our experimental results agreed with the B-H theory for the predicted orientation of the ripple's wave vector in being parallel to the surface component of the beam direction. However, it disagreed in that the roughness and the wavelength do not depend on the areic dose.

It is possible to use the seeding sputter erosion model to explain the initiation of cone formation. In a similar study done by Pan *et. al* [pan 98] they investigated the surface of O_2^+ bombarded InP using XPS. The results indicated that the bombarded surface consist of metallic In clusters, which may act as seeding points having lower sputter yield than the InP surrounding it.

Another possible mechanism for cone formation is the difference in sputter yield between the InP and the InN and the InP nitrides that were reported to exist in N^+ bombarded InP [San 03a], [San 03b].

6.2.4 Periodicity

We examined the periodicity of the surface structures from the AFM images on the basis of 2D FFT (see fig. 5.17 Chapter 5).

The origin of the reciprocal space is located at the center of each spectrum. Fig. 5.17(a) exhibits no significant structures. In fig. 5.17 (b) to (f) we can see two spots located in the equator line, which indicate that the ripple ridges are perpendicular to the incident beam. The spot radius is inversely proportional to the features correlation length. In most of the cases it was impossible to measure the spot radius from the obtained power spectra because the borders of the spots were not defined.

The spot center values increased with increasing the areic dose, strongly suggesting that the average wavelength increase. More experiments using higher areic doses should be done to confirm these results.

All these observations show that the ripple formation was not caused by accidental defects such as particles or original irregularity on the substrate, but mainly by the conditions of the ion beam.

6.2.5 Summary

Generally speaking, there was an increase in the surface roughness with increasing the areic dose. For low doses ($1x10^{14}$ - $1x10^{15}$ ions/cm^2) of 5 keV N_2^+ at 41° it was observed that the surface roughness was approximately the same as that of the virgin InP and some times it is even lower (see figures 5.1, 5.2, 5.3 and figures 5.10 to 5.17). This could be explained as a result of the amorphization of the surface because of low energy ion bombardment as was reported by Bardin *et. al.* [Bar 89].

From figures (5.10, 5.12, 5.13, 5.14 and 5. 16) there was a linear dependence of the roughness parameters on the logarithm of the areic dose. Figures 5.11 and 5.12 are for the results obtained using the fractal dimension analysis. They also showed that increasing the areic dose generally result in increasing the roughness.

In a study done by Treichler *et. al.* as was discussed in [Mal 91] using O_2^+ and Cs^+ to bombard InP substrates it was found the Cs^+ bombarded surfaces was wavy, while the O_2^+ was smooth but the TEM investigation in the same study confirmed the co-existence of amorphous-crystalline regions. Malherbe *et. al.* used STEM to investigate argon bombarded InP and it was found that the surface of ion-bombarded InP consist of re-crystallized and amorphous regions[Mal 91].

6.3 Model for roughness dependence on areic dose

The development of the sputter cones on InP is a complex process and depends on many factors [Mal 94]. Apart from the initial growth phase of these cones, it is expected that the "further" growth of the cone size and height (reflected by the rms roughness and roughness factor behavior) will be inhibited by erosion of the cones through sputtering. The amount of material removed by sputtering is proportional to the areic dose Φ. The erosion- inhibited growth rate of the sputtered cone is therefore given by:

$$\frac{dR_{rms}}{d\Phi} \propto \frac{1}{\Phi} \qquad (1)$$

with the solution;

$$\Phi = \phi e^{\gamma R_{rms}} \qquad (2)$$

Φ : Areic dose (ions/cm^2).

γ : Growth parameter (depends primarily on the bombardment ion species).

ϕ : The threshold areic dose (the minimum areic dose required for the cones to start growing).

Applying this model to our experimental results from figure 5.16 (Chapter 5) from the straight line

$$R_{rms} = m(\log\Phi) + c \qquad (3)$$

and from equation (2);

$$R_{rms} = \frac{\log\Phi}{\gamma} - \frac{\log\phi}{\gamma} \qquad (4)$$

Comparing the two equations (3) and (4) we obtain the values for ϕ and γ to be;

ϕ = 3.26 x 10^{14} N_2^+/cm^2

γ = 0.552 nm^{-1}

Semiconductor surface bombardment by a low energy reactive ion beam exhibits a complex behaviour. This complexity is a result of combined physical and chemical nature of the sputtering.

References: Chapter 6

[Bar 89] T. T. Bardin, J. G. Pronko, A. J. Mardinly and C. R. Wie, *Nucl. Instrum. Meth. Phys. Res.* B (40/41) (1989) 533.

[Bra 88] R. M. Bradley and J. M. E. Harper, *J. Vac. Sci. Technol.* A 6 (1988) 2390.

[Dem 95] C. M. Demanet, J. B. Malherbe, N. G. van der Berg and K. Vijaya Sankar, *Surf. Interface Anal.* 23 (1995) 433.

[Mak 02] M. A. Makeev, R. Cuerno and A.- L. Barabasi, *Nucl. Instrum. Meth. Phys. Res.* B 197 (2002) 185.

[Mal 91] J. B. Malherbe, H. Lanker, and W. H. Gries, *Surf. Interface Anal.* 17 (1991) 719.

[Mal 94] J. B. Malherbe, CRC *Crit. Rev. Solid State Mat. Sci.* 19 (1994) 129.

[Pan 98] J. S. Pan, S. T. Tay, C. H. A. Huan and A. T. S. Wee, *Surf. Interface Anal.* 26 (1998) 930.

[San 03a] K. Santhakumar, P. Jayavel, G. L. N. Reddy, V. S. Sastry, K. G. M. Nair and V. Ravichandran, *Nucl. Instrum. Meth. Phys. Res.* B 212 (2003) 197.

[San 03b] K. Santhakumar, R. Kesavamoorthy, K. G. M. Nair, P. Jayavel, D. Kanjilal, V. Sankara Sastry and V. Ravichandran, *Nucl. Instrum. Meth. Phys. Res.* B 212 (2003) 521.

Chapter 7

Conclusion

7.1 Summary

This work is part of many attempts by this laboratory (UP Surface Science group) to understand the processes responsible for the development of topographical features on semiconductor surfaces after ion bombardment. The effect of N_2^+ areic dose on bombardment-induced topography of InP was studied.

This desertion was organized as the following:

In the beginning we gave an introduction including a general overview of the material and techniques used and the aim and objectives. We gave a general review of the experimental results reported by different research groups on InP and other semiconductors and the topography dependence on the different sputtering parameters. We also reviewed the major theoretical studies and models proposed to describe the morphology of ion-eroded surfaces.

A description of sample preparation, ion bombardment and FE-SEM and AFM systems used was discussed in detail. A comparison was given between the two techniques used (FE-SEM and AFM) and a motivation of the use of the two as complementary techniques in morphology investigations.

FE-SEM and AFM images were presented showing the evolution of surface topographical features with increasing areic dose. Graphs illustrating the behavior of the different roughness parameters reported as functions of areic doses were also presented. FFT was applied to the AFM images for the different doses used to investigate the beginning and development of periodic structures. A comparison was given between the ripple wavelengths for the $1x10^{18}$ and 5×10^{17} N_2^+/cm^2 samples

measured from the AFM original images, after applying 2D fast Fourier transform. A graph showing the wavelengths as a function of the areic dose is also presented

In chapter 6 we gave a discussion of the results and a comparison with another research groups findings. A comparison of the results with the predictions of some of the theories presented in chapter 3 with experimental results on surface roughening and ripple formation was also made.

A theoretical model was proposed in an attempt to predict the evolution of the surface R_{rms} roughness with increasing ion areic dose. This model was tested against the experimental findings.

7.2 Conclusion

Through the above process the following conclusions were arrived at:

- There was an increase in the surface roughness of InP after 5keV N_2^+ bombardment.
- Above a dose of $5x10^{14}$ N_2^+/cm^2 there was a linear relation between the rms roughness (R_{rms}) and the logarithm of the areic dose.

$$R_{rms} \propto \log \Phi$$

- In comparison with the reported results of the effect of areic dose of Ar^+ bombardment on the rms roughness of InP [Dem 95], the reactive N_2^+ bombardment induced topography, showed the same trend.

- The proposed model was found to be in good agreement with the experimental findings.

- From the FFT of the AFM images the periodicity of surface features increase with increasing areic dose.

- It is better to use more than one technique to get more information about the system under investigation.

7.3 Future work

Possibilities for future research can be identified as follows:

- Fixing the areic dose rate and doing the same experiment under the same conditions.
- Bombard the sample starting with the areic dose $1x10^{15}$ N_2^+ / cm^2 and go to higher dose ~ $5x10^{19}$ N_2^+ / cm^2 to investigate the development of the ripples wavelength and amplitude with increasing areic dose.
- Investigate the composition of the surface ripples using a technique like XPS and compare with the recent results from other research groups [Pan 96], [San 03a], [San 03b].

7.4 Project output

- A poster presented in the 8th European Vacuum Congress in Berlin, June 2003 with the title: Dose Dependent Topography of N_2^+ Bombarded InP.
- A paper in process of finalization will be sent for publication.

References: Chapter 7

[Dem 95] C.M. Demanet, J.B. Malherbe, N.G. van der Berg and K.Vijaya Sankar, *Surf. Interface Anal.* 23 (1995) 433.

[Pan 96] J. S. Pan, A. T. S. Wee, C. H. A. Huan, H. S. Tan, K. L. Tan, *J. Phys. D: Appl. Phys.* 29 (1996) 2997.

[San 03a] K. Santhakumar, P. Jayavel, G. L. N. Reddy, V. S. Sastry, K. G. M. Nair, V. Ravichandran, *Nucl. Instrum. Meth. Phys. Res.* B 212 (2003) 197.

[San 03b] K. Santhakumar, R. Kesavamoorthy, K. G. M. Nair, P. Jayavel, D. Kanjilal, V. Sankara Sastry, V. Ravichandran, *Nucl. Instrum. Meth. Phys. Res.* B 212 (2003) 521.